
Stiff Transfer Learning for Physics-Informed Neural Networks

Emilien Seiler*
EPFL

Wanzhou Lei
Harvard University

Pavlos Protopapas
Harvard University

Abstract

Stiff differential equations are prevalent in various scientific domains, posing significant challenges due to the disparate time scales of their components. As computational power grows, physics-informed neural networks (PINNs) have led to significant improvements in modeling physical processes described by differential equations. Despite their promising outcomes, vanilla PINNs face limitations when dealing with stiff systems, known as failure modes. In response, we propose a novel approach, stiff transfer learning for physics-informed neural networks (STL-PINNs), to effectively tackle stiff ordinary differential equations (ODEs) and partial differential equations (PDEs). Our methodology involves training a Multi-Head-PINN in a low-stiff regime, and obtaining the final solution in a high stiff regime by transfer learning. This addresses the failure modes related to stiffness in PINNs while maintaining computational efficiency by computing one-shot solutions. The proposed approach demonstrates superior accuracy and speed compared to PINNs-based methods, as well as comparable computational efficiency with implicit numerical methods in solving stiff-parameterized linear and polynomial nonlinear ODEs and PDEs under stiff conditions. Furthermore, we demonstrate the scalability of such an approach and the superior speed it offers for simulations involving initial conditions and forcing function reparametrization.

1 Introduction

Stiff differential equations present a unique challenge in numerical analysis due to their disparate time scales, where some of their components evolve rapidly while others change slowly. This phenomenon can produce rapid transient phases or highly oscillatory solutions when solving stiff ordinary differential equations (ODEs) and stiff partial differential equations (PDEs). These equations are prevalent in several scientific and engineering domains such as chemistry [Santillana et al., 2016], circuit simulation [Debnath and Chinthavali, 2018] or astrophysics [Saijo, 2018]. Explicit numerical schemes face difficulties with stiffness due to the necessity of employing exceedingly small step sizes for stability [Hairer and Wanner, 1996]. In contrast, implicit methods such as Radau [Hairer and Wanner, 1999] or Runge Kutta fourth-order EDT [Kassam and Trefethen, 2005] are stiffness-accurate methods and provide robust solutions by effectively capturing the stiff dynamics. Although these methods have proven to be successful, they have limitations. For example, they can be quite expensive in terms of computational time, being affected by the so-called "curse of dimensionality" in high-dimensional PDEs [Hammer, 1958].

As computational power grows and machine learning techniques evolve, researchers are turning to data-driven and learning-based approaches to solve PDEs and ODEs. One notable architecture that has recently gained attention is the so-called physics-informed neural networks (PINNs) [Lagaris et al., 1998]. These models use neural networks and gradient-based optimization algorithms, leveraging automatic differentiation to enforce physical constraints. PINNs have been successfully applied to numerous important applications in the field of computational science, including computational fluid dynamics [Jin et al., 2021], quantum mechanics [Shah et al., 2022], cardiac electrophysiology simulation [Sahli Costabal et al., 2020], and material science [Zhang et al., 2022], to name a few. Compared to numerical methods that need to interpolate and store dense meshes, PINNs offer the advantages of rapid evaluations through forward passes and only

need to store the model’s weights. Moreover, PINNs are an alternative when dealing with the ”curse of dimensionality” [Cho et al., 2023a].

Despite the advantages and promising outcomes of PINNs, they face a fundamental limitation regarding stiff systems, known as a ”failure mode” [Krishnapriyan et al., 2021]. Wang et al. [2020] identified a first failure mode linked to numerical stiffness, resulting in imbalanced back-propagated gradients during training. Then, Ji et al. [2021] demonstrated that stiffness primarily causes PINNs to fail in simulating stiff kinetic systems. To address this issue, Baty [2023] proposed straightforward methods to enhance the training process, while Zhao et al. [2024] introduced PINNs-Former, a state-of-the-art Transformer-based framework with multi-head attention and a Wavelet activation function.

However, the previous solutions share a fundamental limitation with PINNs which hinders their applicability to a broader range of applications: it is necessary to train a new neural network from scratch to accommodate a novel parameter set of the equation (e.g., novel initial conditions, forcing function, etc.). Hence, the use of PINNs to solve scenarios that involve numerous queries is often computationally demanding. For example, in design optimization and uncertainty propagation, the parameterized ODEs and PDEs must be simulated thousands of times. As a solution, Cho et al. [2023b] proposed lightweight low-rank PINNs. On the other hand, our contribution is based on transfer learning.

Transfer learning (TL) represents a potential solution to the problem of computing parametrized solutions without the need for retraining. The architecture of multi-head physics-informed neural networks (MH-PINN) enables to learn the ”latent space” of a class of differential equations [Zou and Karniadakis, 2023]. From this, Desai et al. [2022] proposed a transfer learning framework for PINNs, which led to ”one-shot” inference for linear systems of PDEs and ODEs. This implies that highly accurate solutions for numerous unknown differential equations can be obtained instantaneously without retraining the entire network. This transfer learning approach has already been applied to the simulation of branched flows [Pellegri et al., 2022]. Lei et al. [2023] extended this approach to nonlinear ODEs and PDEs with polynomial terms using the perturbation method.

We propose stiff transfer learning for physics-informed neural networks (STL-PINNs), a method tailored to tackle stiffness in ODEs and PDEs. This method unfolds i) training a MH-PINN in a low-stiff regime of the equation, and ii) transfer learning to compute the

solution in a high-stiff regime.

In essence, this method addresses the two critical challenges mentioned before i) PINNs ”failure mode” from stiffness during training, since the base model is trained in a low-stiff regime, and ii) the computational burden of retraining PINNs when changing parameters, as final solutions are computed in ”one-shot transfer learning.

We show the efficacy and efficiency of our proposed method by solving stiff-parametrized linear and nonlinear ODEs and PDEs, such as *duffing equation* or *advection-reaction equation*. Our contributions include:

1. We develop a method based on transfer learning to solve stiff equations by training the model in a least-stiff regime.
2. We demonstrate that the proposed method outperforms state-of-the-art PINNs-based methods in both accuracy and speed, in ”failure modes” associated with stiffness.
3. We show that our method’s computational time is independent of stiffness and faster than the implicit methods for the given examples.
4. We establish that our method is scalable regarding training regimes.
5. We show that the proposed method offers significantly superior speed compared to numerical methods for simulations involving initial conditions or forcing function reparametrization.

2 Preliminary Components

We are interested in linear systems of ODEs and PDEs of the following form:

$$\sum_{j=1}^d C_j \frac{\partial y}{\partial x_j} + B \frac{\partial y}{\partial t} + Ay = f(\mathbf{x}) \quad (1)$$

The PDE in Eq.1 is characterized by the solution $y \in \mathbb{R}^n$. The vector $\mathbf{x} = [t, x_1, \dots, x_d] \in \mathbb{R}^{d+1}$ contains $t \in \mathbb{R}$ the independent variable of time and d the independent variables of spatiality. $A, B, C_k \in \mathbb{R}^{n \times n}$ are coefficient matrices and $f : \mathbb{R}^{d+1} \rightarrow \mathbb{R}^n$ denotes the forcing function. In the subsequent section, the general PDE notation is employed and can be applied to ODEs by setting $d = 0$, $\mathbf{x} = t$ and $\frac{\partial}{\partial t} = \frac{d}{dt}$.

2.1 Multi-Head PINNs

The idea of the MH-PINNs architecture (Fig.1) is to approximate equations of the same form over different

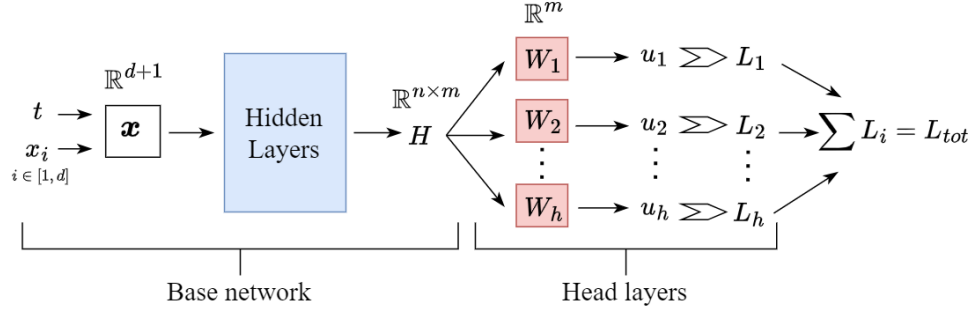


Figure 1: MH-PINNs architecture with h heads. The base network constructs $H \in \mathbb{R}^{n \times m}$ from input \mathbf{x} that passes through multiple hidden layers. m is the dimension of the last hidden layer and n is the dimension of the system of equations. The h head layers consist of separate linear layers W_i without any activation function. Each of them produces individual outputs $u_i = HW_i$ and their loss. These losses are then summed up to yield to the final loss L_{tot} .

parameters. It comprises multiple heads with distinct sets of parameters (e.g., equation coefficients, forcing functions, or initial conditions). Each head is associated with a unique set of weights, W_i , which are used to generate outputs $u_i = HW_i$, using the same H . Hence, it encodes the generalized form of the equation in the latent representation H . The following loss function is applied to each head output:

$$L = \frac{\omega_1}{N_1} \sum_{i=1}^{N_1} \left(\sum_{j=1}^d C_j \left(\frac{\partial u}{\partial x_j} \right)_{\mathbf{x}_i} + B \left(\frac{\partial u}{\partial t} \right)_{\mathbf{x}_i} + A u_{\mathbf{x}_i} - f_{\mathbf{x}_i} \right)^2 + \frac{\omega_2}{N_2} \sum_{i=1}^{N_2} \left(u_{\mathbf{x}_i^b} - y_{\mathbf{x}_i^b} \right)^2 \quad (2)$$

where u is the neural network approximation of the true solution y . N_1 is the number of collocation points and \mathbf{x}_i the i^{th} one. N_2 is the number of boundary or initial conditions collocation points and \mathbf{x}_i^b the i^{th} one. The notation $(\cdot)_{\mathbf{x}}$ indicates the evaluation of the function at the point \mathbf{x} . The residual and boundary conditions are leveraged by weights ω_1 and ω_2 . While training, the network adjusts W_i to suit different parameter sets and converges to a fix H .

2.2 One-Shot Transfer Learning

After training with MH-PINNs, the final value H is saved as H_{fix} . A head layer can be considered as a matrix multiplication operation $u = H_{fix}W$. Then, for untrained heads with different parameters, namely, $\hat{C}_j, \hat{B}, \hat{A}, \hat{f}, \hat{y}_{\mathbf{x}_i^b}$ only W computation is needed. The optimal weight, denoted as \hat{W} , is derived by minimizing the loss function of Eq.2 after substitution of $u = H_{fix}W$. The following Eq.3 is the solution of $\nabla_W L = 0$. Here, H_{fix} is denoted as H for clarity (see

App.A for derivation details):

$$\hat{W} = M^{-1} \left(\frac{\omega_1}{N_1} \sum_{i=1}^{N_1} H_{\mathbf{x}_i}^* T \hat{f}_{\mathbf{x}_i} + \frac{\omega_2}{N_2} \sum_{i=1}^{N_2} H_{\mathbf{x}_i^b}^T \hat{y}_{\mathbf{x}_i^b} \right) \quad (3)$$

$$M = \frac{\omega_1}{N_1} \sum_{i=1}^{N_1} H_{\mathbf{x}_i}^{*T} H_{\mathbf{x}_i}^* + \frac{\omega_2}{N_2} \sum_{i=1}^{N_2} H_{\mathbf{x}_i^b}^T H_{\mathbf{x}_i^b}$$

$$H_{\mathbf{x}_i}^* = \sum_{j=1}^d \hat{C}_j H_{\mathbf{x}_i}^{x_j} + \hat{B} H_{\mathbf{x}_i}^t + \hat{A} H_{\mathbf{x}_i}$$

with $H^{(\cdot)}$ is the derivative with respect to t, x_j

Hence, we can compute the solution of a new parameter set $u = H_{fix} \hat{W}$. In practice, transfer learning to new coefficients \hat{C}_j, \hat{B} and \hat{A} requires the inversion of the M matrix. However, this is not necessary for \hat{f} and $\hat{y}_{\mathbf{x}_i^b}$ because they are independent of M . Consequently, transfer learning to new forcing functions, initial conditions, or boundary conditions requires less computational time.

2.3 Perturbation Method

Nonlinear differential equations do not possess an analytical solution for W . For nonlinearity with polynomial terms, we consider ODEs and PDEs of the following form:

$$\sum_{j=1}^d C_j \frac{\partial y}{\partial x_j} + B \frac{\partial y}{\partial t} + Ay + \beta g(y) = f(\mathbf{x}) \quad (4)$$

with $\beta \in [0, 1]$ and $g : \mathbb{R}^n \rightarrow \mathbb{R}^n$ a nonlinear polynomial function. To remove the nonlinearity in the equation, we approximate the nonlinear term $\beta g(y)$ as a composition of functions using perturbation expansion [Kevorkian and Cole, 1981]. Assuming $y = \sum_{k=0}^{\infty} \beta^k Y_k$, where Y_k are unknown functions of \mathbf{x} , we

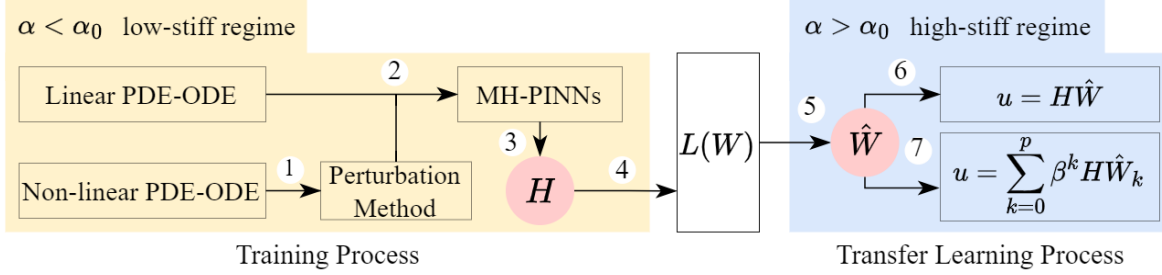


Figure 2: STL-PINN diagram process:

1. Linearize non-linear PDE-ODE.
2. Train MH-PINN in a low-stiff regime.
3. Extract and fix H after training.

4. Substitute $u = HW$ in the loss function.
5. Compute \hat{W} in a high-stiff regime with Eq.3.
- 6&7. Compute final solution u .

approximate y with only p terms as $y \approx \sum_{k=0}^p \beta^k Y_k$. After substitution in Eq.4 and by collecting the power of β , the following formula provides an approximation of the original nonlinear equation (see App.B for derivation details):

$$\sum_{j=1}^d C_j \frac{\partial Y_k}{\partial x_j} + B \frac{\partial Y_k}{\partial t} + AY_k = F_k(\mathbf{x}, Y_0, \dots, Y_{k-1}) \quad (5)$$

$\forall k \in \mathbb{N}, 0 \leq k \leq p$, the forcing function F_k depends only on previously solved Y_0, Y_1, Y_{k-1} . Therefore, Eq.4 is reduced to a series of $p+1$ linear differential equations of the same form.

To perform transfer learning for nonlinear ODEs and PDEs such as Eq.4, we first trained a MH-PINNs on its linear counterpart Eq.5 with $k = 0$. Subsequently, we can use Eq.3 to calculate \hat{W}_k , solving iteratively the series of $p+1$ linear differential equations, and reconstruct the nonlinear solution $u = \sum_{k=0}^p \beta^k H_{\text{fix}} \hat{W}_k$.

2.4 Stiffness Characterization

The term "phenomenon" seems more appropriate than "property," as the latter suggests that stiffness can be precisely defined mathematically, which, unfortunately, is proving difficult. The following statements are used to characterize stiffness:

Stiffness Ratio (SR): Eigenvalues of the Jacobian matrix associated with the system of ODEs that cover a wide range of magnitudes are indicative of stiffness. The following stiffness ratio $SR = \max|\lambda|/\min|\lambda|$ is introduced. If $SR < 20$ the problem is not stiff, from $SR \approx 1000$ the problem is classified as stiff [Lepik and Hein, 2014].

Transient Phase: Stiffness creates rapid transient phases where the rate of change of the solution is significantly higher compared to other time scales [Hairer and Wanner, 1996].

Restricted Stability Regions for Explicit Methods: Stiffness requires very small step sizes for explicit numerical methods to remain stable, making them computationally inefficient [Hairer and Wanner, 1996].

Stiffness in a differential equation can arise based on specific initial conditions, parameters, or regions within the problem space. Although Jacobian eigenvalues certainly contribute to the stiffness of the equation, they often cannot be the only criterion for characterizing stiffness [Higham and Trefethen, 1993]. While SR serves as an indicator of stiffness within an equation, it cannot be extrapolated for comparison between equations because it only captures the effect of the eigenvalues. Quantities such as the dimension of the system, the initial conditions, the forcing function, the smoothness of the solution, or the integration interval must also be considered.

In this work, these three statements are governed by a parameter α . As α increases, the equation becomes stiffer, the SR value increases, the transient phase becomes more rapid, and explicit methods require a longer time to obtain a solution.

3 STL-PINN: Stiff Transfer Learning for Physics-Informed Neural Network

The general idea of the STL-PINN method is to solve stiff equations by transfer learning from a low-stiff regime to a high-stiff regime. Fig.2 explains the overall process of solving stiff-parameterized linear and nonlinear PDEs-ODEs. The key feature of our approach is that the training process is conducted in a low-stiff regime where $\alpha < \alpha_0$, and the final solution is then computed in a high-stiff regime where $\alpha > \alpha_0$. The training heads operate in low-stiff regimes governed by distinct α values. Hence, MH-PINN's latent repre-

sensation H captures variations resulting from changes in the α value, enabling transfer to high-stiff regimes. Moreover, distinct initial conditions or forcing functions can be used on the training heads. This allows the latent representation H to capture variations arising from these changes. After the training process, transfer learning can be applied multiple times across different stiffness regimes and various equation parameter sets (e.g., initial conditions, forcing functions), without the need for retraining. Finally, STL-PINN overcomes the "failure mode" of PINNs associated with training under stiff conditions, and the final solution is computed in "one-shot", making the method computationally efficient.

4 Experiments

We demonstrate that our method significantly outperforms baselines on stiff-parameterized 2-dimensional linear, nonlinear ODEs, and 2-dimensional linear PDE.

Baselines for comparison The objective of this study is to compare the STL-PINN method to vanilla PINN [Lagaris et al., 1998] and the state-of-the-art PINNsFormer [Zhao et al., 2024] models in terms of accuracy and computational time. Additionally, the study aims to compare STL-PINNs with numerical methods, specifically explicit RK45 [Butcher, 1996] and implicit Radau method [Hairer and Wanner, 1999], in terms of computational time.

Accuracy For accuracy metrics, we first employ the L_2 relative error, defined as $L_2^{rel} = \sum_{i=1}^N \sqrt{(u_{\mathbf{x}_i} - y_{\mathbf{x}_i})^2} / \sum_{i=1}^N \sqrt{y_{\mathbf{x}_i}^2}$ being the PINN solution and $y_{\mathbf{x}_i}$ the Radau solution evaluated at \mathbf{x}_i . It offers a measure of the overall performance of the method across all time scales. We also use the L_1 relative error define as $L_1^{rel} = \sum_{i=1}^N |u_{\mathbf{x}_i} - y_{\mathbf{x}_i}| / \sum_{i=1}^N |y_{\mathbf{x}_i}|$. Finally, we use the L_∞ maximum relative error defines as $L_\infty^{rel} = \max_{i \in [1, N]} |u_{\mathbf{x}_i} - y_{\mathbf{x}_i}| / \max_{i \in [1, N]} |y_{\mathbf{x}_i}|$, which serves as an important metric, enhancing the error magnitude caused by rapid transient phases that can occur on a very short time scale.

Computational time STL-PINN objective is to compute multiple solutions of an equation through post-training transfer learning. When discussing computational time, we consider the wall-clock time during the transfer learning phase, after the latent representation H has been exported from training.

4.1 Stiff-parameterized ODEs-PDEs

The following equations are derived from their general representation available in App.C.

2D linear ODEs: For our first stiff-parameterized linear 2-dim ODE, we consider the following overdamped-harmonic-oscillator (OHO) equation:

$$\begin{cases} \frac{dy_1}{dt} - y_2 = 0 & y_1(t=0) = y_{1_0} \\ \frac{dy_2}{dt} + y_1 + \alpha y_2 = 0 & y_2(t=0) = y_{2_0} \end{cases}, t \in [0, T], \quad (6)$$

where y_1 describes the motion of a harmonic oscillator slowed by a frictional force proportional to y_2 , the velocity of the motion. The stiffness parameter α governs the stiffness of the equation and SR is proportional to α^2 . The range of $\alpha > 30$ poses a significant challenge in training vanilla PINNs due to the rapid transient phase in the vicinity of $y_2(t=0)$ caused by the stiffness.

For our second stiff-parameterized linear 2-dim ODE, we consider the following linear ODEs with non-constant forcing function (NCF) [Anne Kvrn, 2020]:

$$\begin{cases} \frac{dy_1}{dt} + 2y_1 - y_2 = 2 \sin(\omega t) \\ \frac{dy_2}{dt} + (1 - \alpha) y_1 + \alpha y_2 = \alpha (\cos(\omega t) - \sin(\omega t)) \\ \text{with } y_1(t=0) = y_{1_0}, y_2(t=0) = y_{2_0} \end{cases} \quad (7)$$

where y_1, y_2 describe an oscillation motion governed by the angular frequency ω with a rapid transient phase in the vicinity of $t=0$. SR is proportional to α and values of $\alpha > 30$ pose a significant challenge in training vanilla PINNs.

2D nonlinear ODE: For a stiff-parameterized nonlinear polynomial 2-dim ODE, we consider the following Duffing equation:

$$\begin{cases} \frac{dy_1}{dt} - y_2 = 0 \\ \frac{dy_2}{dt} + y_1 + \alpha y_2 + \beta y_1^3 = \cos(t) \\ \text{with } y_1(t=0) = y_{1_0}, y_2(t=0) = y_{2_0} \end{cases} \quad (8)$$

with $\beta \in]0, 1[$ and y_1 describes the motion of a damped oscillator with a more complex potential due to a periodic driving force and the β term that controls the amount of nonlinearity in the restoring force. SR is proportional to α^2 . For $\alpha > 40$, vanilla PINNs training faces challenges due to rapid transient phases near $y_2(t=0)$.

2D linear PDE: For a stiff-parameterized PDE we consider the 2-dim linear advection-reaction equation (AR):

$$\begin{cases} \frac{dy_1}{dt} + \mu \frac{dy_1}{dx} + \alpha (k_1 y_1 - k_2 y_2) = 0 \\ \frac{dy_2}{dt} + \mu \frac{dy_2}{dx} - \alpha (k_1 y_1 - k_2 y_2) = 0 \\ t \in [0, T], x \in [0, L], \end{cases} \quad (9)$$

with $y_1(t, x=0) = y_1(t, x=L) = 0$,
 $y_2(t, x=0) = y_2(t, x=L) = 0$,
 $y_1(t=0, x) = y_{1_0}(x)$, $y_2(t=0, x) = y_{2_0}(x)$, clamped
 cubic spline with maximum value y_0^{max} .

This system comes from the advection-reaction atmospheric equation. It is characterized by the evolution of chemical species in a constant wind field with stiff chemistry mechanisms. As investigated by Santillana et al. [2016], the stiffness comes from the reaction dynamics being much faster than the advection one. The parameters are set to $\mu = 1.8 \times 10^{-4}$, $k_1 = 1 \times 10^{-3}$, $k_2 = 2 \times 10^{-3}$ with effective stiffness of the order $\mathcal{O}(10^{-1})$. The stiffness is governed by α that changes the dynamics of the chemical reaction. For $\alpha > 30$ vanilla PINNs struggle because of a rapid transient phase when the chemical components reach equilibrium. For numerical simulations, we used Godunov splitting and implemented an explicit second-order accurate (in space) method based on the LaxWendroff (LW) scheme with superbee slope limiters [LeVeque, 2002]. For the chemistry, we used the implicit Radau method.

4.2 Experimental setup

Performance analysis We aim to investigate the performance of STL-PINNs in terms of accuracy and computational time. To achieve this, Table 1 presents the training head configurations of MH-PINN in a low-stiff regime of the ODEs and PDEs. In the case of the Duffing equation, the choice of the perturbation parameter p is optimized within the range $p \in [0, 20]$, as detailed in App.D. Training setup including optimization, loss and model parameters are available in App.E.

Table 1: MH-PINN training heads

	Head	1	2	3	4	5	6	7	8	9	10
OHO	α	2	4	6	8	10	12	14	16	18	20
	y_0	[1, 0.5] for all heads									
NCFE	α	2	4	6	8	10	12	14	16	18	20
	y_0	[2, 4] for all heads									
	ω	1 for all heads									
Duffing	α	13	16	19	22	25	28	31	34	37	40
	y_0	[1, 0.5] for all heads									
	β	0.5 for all heads									
AR	α	3	6	8	12	-	-	-	-	-	-
	y_0^{max}	1	1	1	1	-	-	-	-	-	-

Scalability Analysis We aim to investigate the scalability of STL-PINN in the stiff transfer regime relative to the training one. To achieve this, we trained multiple MH-PINNs with increasing ranges of α values up to α_{max} . Then, we analyze the resulting variations in transfer learning accuracy. Training head configurations are available in App.F.

Reparametrization Analysis We aim to evaluate the performance of STL-PINN in the reparametrization of initial conditions or forcing functions within a stiff regime. These components do not necessitate the inversion of the M matrix (see Eq.3) during the transfer learning phase, thereby offering efficient computational times. To conduct this analysis, we trained a MH-PINN in a low-stiff regime with various initial conditions or forcing functions to capture their behaviors. Then, we conducted 1000 simulations of transfer learning in a high-stiff regime by varying these parameters and reported the average time and accuracy metrics. For OHO, Duffing, and AR equations, the initial conditions vary within specific ranges: $y_{1_0} \in [0, 5]$ and $y_{2_0} \in [0, 5]$ for OHO, $y_{1_0} \in [0.5, 2]$ and $y_{2_0} \in [0, 1]$ for Duffing, $y_0^{max} \in [0.5, 2]$ for AR. On the other hand, the forcing function varies within the interval $\omega \in [0, \pi]$ for the NCFE. Training head configurations are available in App.G.

4.3 Experimental results

Performance analysis: Accuracy Fig.3 shows examples of training and transfer solutions. As expected, training solutions are well aligned with Radau solutions, as they are computed in a low-stiff regime. Moreover, STL-PINNs solutions computed by transfer learning in a high-stiff regime are also accurate. In contrast to vanilla PINNs, our method effectively captures stiff behavior, as evidenced by its precise encoding of sharp transient phases in the vicinity of initial conditions. Vanilla PINNs do not adequately capture these rapid transient phases because of the "failure mode" caused by stiffness. More figures about training and transfer learning solutions are provided in App.H.

Fig.4 compares STL-PINN, vanilla PINN, and PINNsFormer. Vanilla PINN and PINNsFormer fail to encode stiffness, with significant errors appearing at $\alpha = 30$ for OHO, $\alpha = 20$ for NCFE, $\alpha = 40$ for Duffing, and $\alpha = 30$ for AR. STL-PINN consistently outperforms these methods across all α values, with performance improvement of at least an order of magnitude, even in high-stiffness regimes. While STL-PINNs error increases with stiffness, it remains more accurate than other PINNs. Thus, we demonstrate that the STL-PINN method can capture stiffness and obtain accurate solutions over "failure modes" of PINN. The scalability analysis further discusses the limits of transfer learning, and additional metrics are in App.I.

Performance analysis: Computational time Table 2 compares the wall-clock time of STL-PINN with numerical methods. As expected, explicit RK45's computational time significantly increases from 10^{-2} to 10^{-1} seconds as α rises from 20 to 200. In contrast,

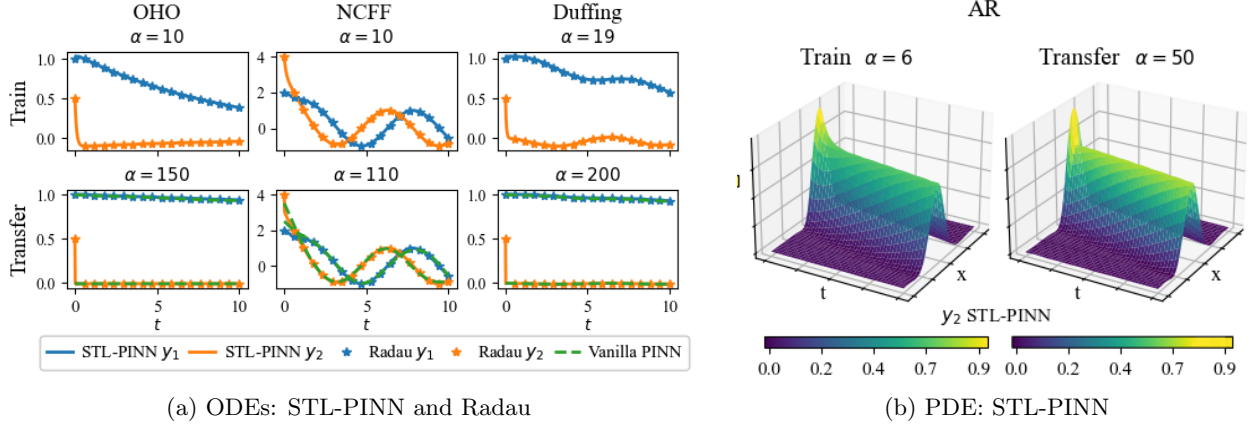


Figure 3: Results for (a) OHO, NCFE, Duffing ODEs (b) AR PDE. For each equation, an example of both training low-stiff and transfer high-stiff STL-PINN solutions is shown. Low-stiff regimes take $\alpha = \{10, 10, 19, 6\}$ while high-stiff regimes take $\alpha = \{150, 110, 200, 50\}$ for OHO, NCFE, Duffing, AR respectively. Additionally for ODEs, the Radau solution is plotted as an accurate approximation and the vanilla PINN solution is provided for the high-stiff regimes.

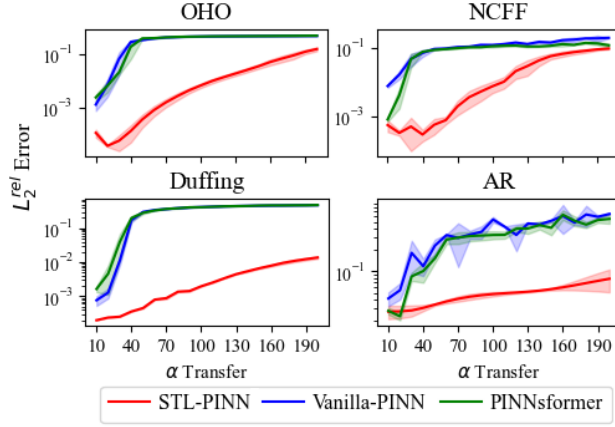


Figure 4: L_2 relative error of vanilla PINN, PINNsFormer and STL-PINN solving stiff-parameterized ODEs-PDEs as stiffness regime increases, with $\alpha \in [10, 200]$. The reported errors are the average of three separate runs, along with 90% confidence intervals.

STL-PINN and Radau maintain consistent computational times regardless of the equation’s stiffness. For ODEs, STL-PINN is faster than Radau, with times in the range of 10^{-3} against 10^{-2} seconds. For the AR equation, our method is significantly faster than LW-Radau, with times in the range of 10^{-2} against 10^1 seconds.

Scalability Analysis Fig.6 illustrates that with a larger training range for , STL-PINN can transfer to higher stiff regimes with reduced error. Indeed, across all equations, larger α_{max} results in a lower error curve and enables transfer learning to stiffer regimes while

maintaining the same error magnitude. For example, with the Duffing equation, we reach 10^{-4} error at $\alpha = 60$ with $\alpha_{max} = 20$. Then, doubling α_{max} to 40, we can now transfer to $\alpha = 140$ with the same 10^{-4} error. More metrics are available in App.J. This demonstrates the scalability of our method: the more we train in stiff regimes, the more we extend the range of transfer learning to even stiffer regimes.

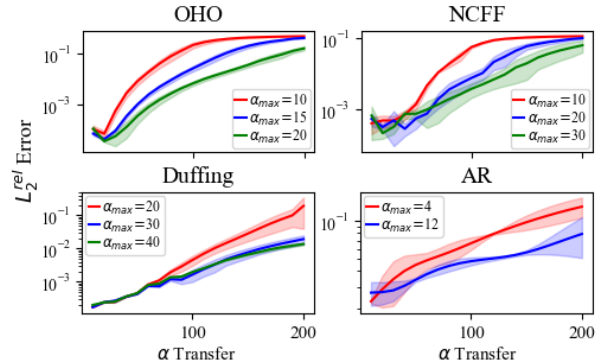


Figure 5: L_2 relative error of STL-PINN over increasing ranges of α during training, where α_{max} denotes the maximum value. The x-axis is the α transfer range. The reported errors are the average of three separate runs, along with 90% confidence intervals.

Table 2: Average wall-clock time over 100 runs of STL-PINN, RK45, Radau and LW-Radau methods solving stiff-parametrized ODEs-PDEs as stiffness regime increases, $\alpha \in [10, 200]$.

α	OHO			NCFE			Duffing			AR	
	STL-PINN	Radau	RK45	STL-PINN	Radau	RK45	STL-PINN	Radau	RK45	STL-PINN	LW-Radau
	<i>Time sec.</i>			<i>Time sec.</i>			<i>Time sec.</i>			<i>Time sec.</i>	
20	0.0033	0.014	0.026	0.0026	0.011	0.017	0.0041	0.012	0.016	0.046	57
50	0.0030	0.016	0.028	0.0026	0.013	0.034	0.0038	0.010	0.031	0.046	57
100	0.0032	0.020	0.051	0.0029	0.011	0.063	0.0042	0.010	0.057	0.046	57
150	0.0035	0.017	0.073	0.0029	0.012	0.092	0.0033	0.010	0.089	0.046	58
200	0.0031	0.018	0.092	0.0025	0.013	0.11	0.0029	0.010	0.11	0.046	58

Reparametrization Analysis Training outcomes on the reparametrization analysis are available in App.K. Table 3 displays the time and accuracy of the reparametrization analysis. Here, STL-PINN performed reparametrization accurately, with mean absolute error comparable to the one involving only a change in stiffness regime. Additionally, we observe that for ODEs, the wall-clock time order of STL-PINN is 10^{-4} seconds. Then, our method is faster than both RK45 and Radau by three and two magnitude orders respectively. Regarding the AR equation, STL-PINN is notably faster than the LW-Radau method, with wall-clock time smaller than four magnitude orders.

Table 3: Average wall-clock time solving 1000 simulations in a high-stiff regime, involving initial conditions or forcing function reparametrization. The mean absolute error of STL-PINN is also provided. Please note that LW-Radau is used for symbol *.

α	OHO	NCFE	Duffing	AR
	150	110	150	100
<i>Time sec.</i>				
STL-PINN	0.00015	0.00081	0.0031	0.0052
Radau	0.016	0.014	0.010	
RK45	0.091	0.076	0.091	58*
MAE	2.3×10^{-3}	1.2×10^{-2}	6.5×10^{-4}	1.6×10^{-2}

5 Limitations and Future Works

We applied STL-PINN using the perturbation method to a nonlinear example, the Duffing equation. However, in some stiff problems, such as the van der Pol equation [Brugnano et al., 2009], there is no finite perturbation solution. To address this, instead of computing the final layer W in "one-shot", we could approximate it using an optimization algorithm such as LBFGS [Berahas et al., 2016]. Since the base network H remains fixed, optimizing only the last layer would produce relatively rapid evaluations.

Although the need to linearize nonlinear PDEs introduces potential errors, complicating the assessment of the method's effectiveness.

We can compute accurate solutions in stiff regimes, challenges arise with extremely stiff regimes, such as $\alpha=1000$. Scalability analysis shows that the more we train in stiff regimes, the more we extend the range of transfer learning to even stiffer regimes. Therefore, for very high-stiff regimes, we need a model capable of training within an already stiff regime. One solution might involve modifying the MH-PINN architecture or training process to mitigate the stiffness "failure mode" [Wang et al., 2020], enabling transfer to very high-stiff regimes.

Our STL-PINN mainly concentrates on cases of stiffness involving a rapid transient phase. In future studies, our framework could be extended to highly oscillatory solutions caused by stiffness.

6 Conclusion

We proposed STL-PINN, a simple yet powerful method that employs transfer learning to solve stiff-parameterized ODEs and PDEs. Experimental results showed that our method can solve stiff equations with high precision, even in PINN's "failure modes". The present method outperform state-of-the-art PINNs-Former method in term of accuracy, while being faster than numerical methods. These performance results pave the way for the application of our method in experiments involving numerous simulations. We believe that this work highlights the potential of PINNs transfer learning in various scientific applications.

References

- Anne Kvrn, M. G. (2020). Stiff differential equations.
- Baty, H. (2023). Solving stiff ordinary differential equations using physics informed neural networks (pinns): simple recipes to improve training of vanilla-pinns.
- Berahas, A. S., Nocedal, J., and Takac, M. (2016). A multi-batch l-bfgs method for machine learning. In Lee, D., Sugiyama, M., Luxburg, U., Guyon, I., and Garnett, R., editors, *Advances in Neural Information Processing Systems*, volume 29. Curran Associates, Inc.
- Brugnano, L., Mazzia, F., and Trigiante, D. (2009). Fifty years of stiffness. *Recent Advances in Computational and Applied Mathematics*.
- Butcher, J. (1996). A history of runge-kutta methods. *Applied Numerical Mathematics*, 20(3):247–260.
- Cho, J., Nam, S., Yang, H., Yun, S.-B., Hong, Y., and Park, E. (2023a). Separable physics-informed neural networks.
- Cho, W., Lee, K., Rim, D., and Park, N. (2023b). Hypernetwork-based meta-learning for low-rank physics-informed neural networks.
- Debnath, S. and Chinthavali, M. (2018). Numerical-stiffness-based simulation of mixed transmission systems. *IEEE Transactions on Industrial Electronics*, 65(12):9215–9224.
- Desai, S., Mattheakis, M., Joy, H., Protopapas, P., and Roberts, S. (2022). One-shot transfer learning of physics-informed neural networks.
- Hairer, E. and Wanner, G. (1996). *Solving Ordinary Differential Equations II. Stiff and Differential-Algebraic Problems*, volume 14.
- Hairer, E. and Wanner, G. (1999). Stiff differential equations solved by radau methods. *Journal of Computational and Applied Mathematics*, 111(1):93–111.
- Hammer, P. C. (1958). *dynamic programming*. richard bellman. princeton university press, princeton, n.j., 1957. xxv+ 342 pp. \$6.75. *Science*, 127(3304):976–976.
- Higham, D. J. and Trefethen, L. N. (1993). Stiffness of odes. *BIT Numerical Mathematics*, 33(2):285–303.
- Ji, W., Qiu, W., Shi, Z., Pan, S., and Deng, S. (2021). Stiff-pinn: Physics-informed neural network for stiff chemical kinetics. *The Journal of Physical Chemistry A*, 125(36):80988106.
- Jin, X., Cai, S., Li, H., and Karniadakis, G. E. (2021). Nsfnets (navier-stokes flow nets): Physics-informed neural networks for the incompressible navier-stokes equations. *Journal of Computational Physics*, 426:109951.
- Kassam, A.-K. and Trefethen, L. N. (2005). Fourth-order time-stepping for stiff pdes. *SIAM Journal on Scientific Computing*, 26(4):1214–1233.
- Keivorkian, J. and Cole, J. (1981). *Perturbation Methods in Applied Mathematics*. Applied Mathematical Sciences. Springer.
- Krishnapriyan, A. S., Gholami, A., Zhe, S., Kirby, R. M., and Mahoney, M. W. (2021). Characterizing possible failure modes in physics-informed neural networks.
- Lagaris, I., Likas, A., and Fotiadis, D. (1998). Artificial neural networks for solving ordinary and partial differential equations. *IEEE Transactions on Neural Networks*, 9(5):987–1000.
- Lei, W., Protopapas, P., and Parikh, J. (2023). One-shot transfer learning for nonlinear odes.
- Lepik, . and Hein, H. (2014). *Stiff Equations*, pages 45–57.
- LeVeque, R. J. (2002). *High-Resolution Methods*, page 100128. Cambridge Texts in Applied Mathematics. Cambridge University Press.
- Pellegrin, R., Bullwinkel, B., Mattheakis, M., and Protopapas, P. (2022). Transfer learning with physics-informed neural networks for efficient simulation of branched flows.
- Sahli Costabal, F., Yang, Y., Perdikaris, P., Hurtado, D. E., and Kuhl, E. (2020). Physics-informed neural networks for cardiac activation mapping. *Frontiers in Physics*, 8.
- Saijo, M. (2018). Determining the stiffness of the equation of state using low dynamical instabilities in differentially rotating stars. *Physical Review D*, 98(2).
- Santillana, M., Zhang, L., and Yantosca, R. (2016). Estimating numerical errors due to operator splitting in global atmospheric chemistry models: Transport and chemistry. *Journal of Computational Physics*, 305:372–386.
- Shah, K., Stiller, P., Hoffmann, N., and Cangi, A. (2022). Physics-informed neural networks as solvers for the time-dependent schrödinger equation.
- Wang, S., Teng, Y., and Perdikaris, P. (2020). Understanding and mitigating gradient pathologies in physics-informed neural networks.
- Zhang, E., Dao, M., Karniadakis, G. E., and Suresh, S. (2022). Analyses of internal structures and defects in materials using physics-informed neural networks. *Science Advances*, 8(7):eabk0644.
- Zhao, Z., Ding, X., and Prakash, B. A. (2024). Pinnsformer: A transformer-based framework for physics-informed neural networks.

Zou, Z. and Karniadakis, G. (2023). L-hydra: Multi-head physics-informed neural networks.

A Derivation of One-Shot TL Weight \hat{W}

A.1 Linear PDE General Case

Following Section.2.2, after substitution of $u = H_{fix}W$, the loss function Eq.2 for an untrained head with parameters $\hat{C}_j, \hat{B}, \hat{A}, \hat{f}, \hat{y}_{\mathbf{x}_i^b}$ is a quadratic function with respect to the head layer weights W (H_{fix} denoted as H for clarity).

$$L(W) = \frac{\omega_1}{N_1} \sum_{i=1}^{N_1} \left(\sum_{j=1}^d \hat{C}_j H_{\mathbf{x}_i}^{x_j} W + \hat{B} H_{\mathbf{x}_i}^t W + \hat{A} H_{\mathbf{x}_i} W - \hat{f}_{\mathbf{x}_i} \right)^2 + \frac{\omega_2}{N_2} \sum_{i=1}^{N_2} \left(H_{\mathbf{x}_i^b} W - \hat{y}_{\mathbf{x}_i^b} \right)^2$$

- N_1 is the number of collocation points
- \mathbf{x}_i the i^{th} collocation point
- N_2 is the number of boundary/initial conditions collocation points
- \mathbf{x}_i^b the i^{th} boundary/initial conditions collocation points
- $(\cdot)_{\mathbf{x}}$ evaluation of (\cdot) at \mathbf{x}
- $H^{(\cdot)}$ the derivative of H with respect to (\cdot)
- ω_1 weight of ODE / PDE loss
- ω_2 weight of boundary/initial conditions loss

Thus $u_{\mathbf{x}_i} = H_{\mathbf{x}_i} W$, $\left(\frac{\partial u}{\partial x_j}\right)_{\mathbf{x}_i} = H_{\mathbf{x}_i}^{x_j} W$, $\left(\frac{\partial u}{\partial t}\right)_{\mathbf{x}_i} = H_{\mathbf{x}_i}^t W$.

With dimensions:

- $\mathbf{x}_i, \mathbf{x}_i^b \in \mathbb{R}^{d+1}$
- $H_{\mathbf{x}_i}, H_{\mathbf{x}_i}^{x_j}, H_{\mathbf{x}_i}^t \in \mathbb{R}^{n \times m}$
- $W \in \mathbb{R}^m$
- $\hat{C}_j, \hat{B}, \hat{A} \in \mathbb{R}^{n \times n}$
- $\hat{f}, \hat{y}_{\mathbf{x}_i^b} \in \mathbb{R}^n$
- m is the dimension of the last hidden layer of the base network
- n the ODE / PDE system's dimension

Let's simplify the expression by introducing the variable H^* :

$$H_{\mathbf{x}_i}^* = \sum_{j=1}^d \hat{C}_j H_{\mathbf{x}_i}^{x_j} + \hat{B} H_{\mathbf{x}_i}^t + \hat{A} H_{\mathbf{x}_i}$$

After substitution of H^* into the loss:

$$L(W) = \frac{\omega_1}{N_1} \sum_{i=1}^{N_1} \left(H_{\mathbf{x}_i}^* W - \hat{f}_{\mathbf{x}_i} \right)^2 + \frac{\omega_2}{N_2} \sum_{i=1}^{N_2} \left(H_{\mathbf{x}_i^b} W - \hat{y}_{\mathbf{x}_i^b} \right)^2$$

Taking the gradient of L with respect to W :

$$\nabla_W L(W) = \frac{2\omega_1}{N_1} \sum_{i=1}^{N_1} \left(H_{\mathbf{x}_i}^{*T} \left(H_{\mathbf{x}_i}^* W - \hat{f}_{\mathbf{x}_i} \right) \right) + \frac{2\omega_2}{N_2} \sum_{i=1}^{N_2} \left(H_{\mathbf{x}_i^b}^T \left(H_{\mathbf{x}_i^b} W - \hat{y}_{\mathbf{x}_i^b} \right) \right)$$

We want \hat{W} such that $\nabla_W L(\hat{W}) = 0$:

$$\frac{\omega_1}{N_1} \sum_{i=1}^{N_1} \left(H_{\mathbf{x}_i}^{*T} \left(H_{\mathbf{x}_i}^* \hat{W} - \hat{f}_{\mathbf{x}_i} \right) \right) + \frac{\omega_2}{N_2} \sum_{i=1}^{N_2} \left(H_{\mathbf{x}_i^b}^T \left(H_{\mathbf{x}_i^b} \hat{W} - \hat{y}_{\mathbf{x}_i^b} \right) \right) = 0$$

Bringing \hat{W} terms on one side of the equation:

$$\frac{\omega_1}{N_1} \sum_{i=1}^{N_1} \left(H_{\mathbf{x}_i}^{*T} H_{\mathbf{x}_i}^* \right) \hat{W} + \frac{\omega_2}{N_2} \sum_{i=1}^{N_2} \left(H_{\mathbf{x}_i^b}^T H_{\mathbf{x}_i^b} \right) \hat{W} = \frac{\omega_1}{N_1} \sum_{i=1}^{N_1} \left(H_{\mathbf{x}_i}^{*T} \hat{f}_{\mathbf{x}_i} \right) + \frac{\omega_2}{N_2} \sum_{i=1}^{N_2} \left(H_{\mathbf{x}_i^b}^T \hat{y}_{\mathbf{x}_i^b} \right)$$

Regrouping \hat{W} terms:

$$\left(\frac{\omega_1}{N_1} \sum_{i=1}^{N_1} \left(H_{\mathbf{x}_i}^{*T} H_{\mathbf{x}_i}^* \right) + \frac{\omega_2}{N_2} \sum_{i=1}^{N_2} \left(H_{\mathbf{x}_i^b}^T H_{\mathbf{x}_i^b} \right) \right) \hat{W} = \frac{\omega_1}{N_1} \sum_{i=1}^{N_1} \left(H_{\mathbf{x}_i}^{*T} \hat{f}_{\mathbf{x}_i} \right) + \frac{\omega_2}{N_2} \sum_{i=1}^{N_2} \left(H_{\mathbf{x}_i^b}^T \hat{y}_{\mathbf{x}_i^b} \right)$$

Introducing the variable $M \in \mathbb{R}^{m \times m}$:

$$M = \frac{\omega_1}{N_1} \sum_{i=1}^{N_1} \left(H_{\mathbf{x}_i}^{*T} H_{\mathbf{x}_i}^* \right) + \frac{\omega_2}{N_2} \sum_{i=1}^{N_2} \left(H_{\mathbf{x}_i^b}^T H_{\mathbf{x}_i^b} \right)$$

Substituting M into the equation, we get the same weight \hat{W} as Eq.3:

$$\hat{W} = M^{-1} \left(\frac{\omega_1}{N_1} \sum_{i=1}^{N_1} \left(H_{\mathbf{x}_i}^{*T} \hat{f}_{\mathbf{x}_i} \right) + \frac{\omega_2}{N_2} \sum_{i=1}^{N_2} \left(H_{\mathbf{x}_i^b}^T \hat{y}_{\mathbf{x}_i^b} \right) \right)$$

A.2 Linear ODE Special Case

In an ODE, there is only one independent variable t so the variable H^* is:

$$H_{t_i}^* = \hat{B} H_{t_i}^t + \hat{A} H_{t_i}$$

There is also only one initial condition collocation point so $N_2 = 1$ and $\mathbf{x}_i^b = t_0$. Then, M is reduced to:

$$M_{ode} = \frac{\omega_1}{N_1} \sum_{i=1}^{N_1} \left(H_{t_i}^{*T} H_{t_i}^* \right) + \omega_2 H_{t_0}^T H_{t_0}$$

Thus, \hat{W} formula becomes:

$$\hat{W}_{ode} = M^{-1} \left(\frac{\omega_1}{N_1} \sum_{i=1}^{N_1} \left(H_{t_i}^{*T} \hat{f}_{t_i} \right) + \omega_2 H_{t_0}^T \hat{y}_{t_0} \right)$$

B Derivation of Linear Systems after Perturbation Expansion

We start with the nonlinear equation representation:

$$\sum_{j=1}^d C_j \frac{\partial y}{\partial x_j} + B \frac{\partial y}{\partial t} + Ay + \beta g(y) = f(\mathbf{x})$$

with $\beta \in [0, 1]$ and $g : \mathbb{R}^n \rightarrow \mathbb{R}^n$ a nonlinear polynomial function.

After perturbation expansion $y \approx \sum_{k=0}^p \beta^k Y_k$:

$$\sum_{j=1}^d \left(C_j \sum_{k=0}^p \beta^k \frac{\partial Y_k}{\partial x_j} \right) + B \sum_{k=0}^p \beta^k \frac{\partial Y_k}{\partial t} + A \sum_{k=0}^p \beta^k Y_k + \beta g \left(\sum_{k=0}^p \beta^k Y_k \right) = f(\mathbf{x})$$

After substitution of g a polynomial nonlinear equation $g(y) = y^q$:

$$\sum_{j=1}^d \left(C_j \sum_{k=0}^p \beta^k \frac{\partial Y_k}{\partial x_j} \right) + B \sum_{k=0}^p \beta^k \frac{\partial Y_k}{\partial t} + A \sum_{k=0}^p \beta^k Y_k + \beta \left(\sum_{k=0}^p \beta^k Y_k \right)^q = f(\mathbf{x})$$

Using the multinomial theorem:

$$\left(\sum_{k=0}^p \beta^k Y_k \right)^q = \sum_{l_0+l_1+\dots+l_p=q} \frac{q!}{l_0!l_1!\dots l_p!} \beta^{\sum_{n=0}^p n l_n} \prod_{k=0}^p Y_k^{l_k}$$

Substituting into the equation:

$$\sum_{j=1}^d \left(C_j \sum_{k=0}^p \beta^k \frac{\partial Y_k}{\partial x_j} \right) + B \sum_{k=0}^p \beta^k \frac{\partial Y_k}{\partial t} + A \sum_{k=0}^p \beta^k Y_k + \beta \left(\sum_{l_0+l_1+\dots+l_p=q} \frac{q!}{l_0!l_1!\dots l_p!} \beta^{\sum_{n=0}^p n l_n} \prod_{k=0}^p Y_k^{l_k} \right) = f(\mathbf{x})$$

Collecting the first power of β into linear systems:

$$\beta^0 : \sum_{j=1}^d \left(C_j \frac{\partial Y_0}{\partial x_j} \right) + B \frac{\partial Y_0}{\partial t} + A Y_0 = f(\mathbf{x})$$

$$\beta^1 : \sum_{j=1}^d \left(C_j \frac{\partial Y_1}{\partial x_j} \right) + B \frac{\partial Y_1}{\partial t} + A Y_1 = -Y_0^q$$

$$\beta^2 : \sum_{j=1}^d \left(C_j \frac{\partial Y_2}{\partial x_j} \right) + B \frac{\partial Y_2}{\partial t} + A Y_2 = -q Y_0^{q-1} Y_1$$

Generalizing for β^k with $k \in \mathbb{N}$, $0 \leq k \leq p$ gives $p + 1$ linear systems of the form:

$$\sum_{j=1}^d C_j \frac{\partial Y_k}{\partial x_j} + B \frac{\partial Y_k}{\partial t} + A Y_k = F_k(\mathbf{x}, Y_0, \dots, Y_{k-1})$$

with

$$F_0 = f(\mathbf{x}), \quad F_k = - \sum_{\substack{l_0+l_1+\dots+l_p=q \\ \sum_{n=0}^p n l_n = k-1}} \frac{q!}{l_0!l_1!\dots l_p!} \prod_{k=0}^p Y_k^{l_k}$$

with the forcing function F_k depending on the previous Y_0, Y_1, Y_{k-1} solutions. The derivation of Eq.5 is then presented.

C General Representation of ODEs and PDEs

In this section we introduce the ODEs and PDEs examples in the general form of Eq.1. As a reminder we are interested in linear systems of ODEs and PDEs of the following form:

$$\sum_{j=1}^d C_j \frac{\partial y}{\partial x_j} + B \frac{\partial y}{\partial t} + A y = f(\mathbf{x})$$

C.1 OHO

$$y = [y_1, y_2]^T \in \mathbb{R}^2, \quad d = 0, \quad \mathbf{x} = t \in \mathbb{R}$$

$$B = \begin{bmatrix} 1 & 0 \\ 0 & 1 \end{bmatrix}, \quad A = \begin{bmatrix} 0 & -1 \\ 1 & \alpha \end{bmatrix}, \quad f(t) = \begin{bmatrix} 0 \\ 0 \end{bmatrix}$$

C.2 NCFF

$$y = [y_1, y_2]^T \in \mathbb{R}^2, \quad d = 0, \quad \mathbf{x} = t \in \mathbb{R}$$

$$B = \begin{bmatrix} 1 & 0 \\ 0 & 1 \end{bmatrix}, \quad A = \begin{bmatrix} 2 & -1 \\ 1 - \alpha & \alpha \end{bmatrix}, \quad f(t) = \begin{bmatrix} 2\sin(\omega t) \\ \alpha(\cos(\omega t) - \sin(\omega t)) \end{bmatrix}$$

C.3 Duffing

Because of the nonlinearity, we take Eq.4 as a reference which adds the non-linear function g :

$$y = [y_1, y_2]^T \in \mathbb{R}^2, \quad d = 0, \quad \mathbf{x} = t \in \mathbb{R}$$

$$B = \begin{bmatrix} 1 & 0 \\ 0 & 1 \end{bmatrix}, \quad A = \begin{bmatrix} 0 & -1 \\ 0.1 & \alpha \end{bmatrix}, \quad g(y) = \begin{bmatrix} 0 \\ y_1^3 \end{bmatrix}, \quad f(t) = \begin{bmatrix} 0 \\ \cos(t) \end{bmatrix}$$

C.4 AR

$$y = [y_1, y_2]^T \in \mathbb{R}^2, \quad d = 1, \quad \mathbf{x} = [t, x]^T \in \mathbb{R}^2$$

$$C_1 = \begin{bmatrix} \mu & 0 \\ 0 & \mu \end{bmatrix}, \quad B = \begin{bmatrix} 1 & 0 \\ 0 & 1 \end{bmatrix}, \quad A = \begin{bmatrix} \alpha k_1 & -\alpha k_2 \\ -\alpha k_1 & \alpha k_2 \end{bmatrix}, \quad f(t) = \begin{bmatrix} 0 \\ 0 \end{bmatrix}$$

D Perturbation Expansion Parameter p Optimization

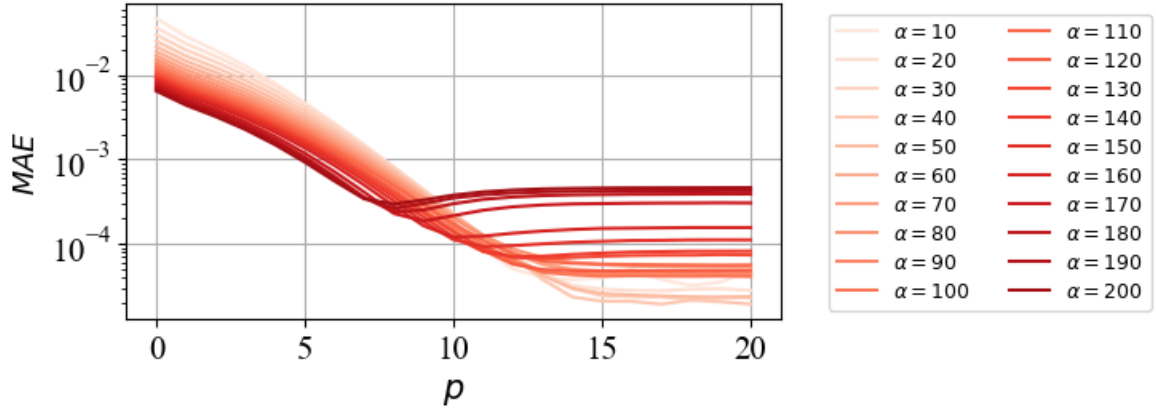


Figure 6: Mean absolute error of STL-PINN with $p \in [0, 20]$ and $\alpha \in [10, 200]$, solving the Duffing equation.

In the case of the Duffing equation, we need to choose a perturbation parameter p since it is a nonlinear equation. For each value of α in Figure 6, the optimal value p_{opt} is identified as the one that minimizes the mean absolute error of $p \in [0, 20]$.

E Optimization, Loss, Model and Compute Resources Settings

The optimization algorithm employed is Adam, with a learning rate decay of γ applied to each parameter group every step-size epoch. The loss function comes from Eq.2 and the model is MH-PINN. The following table presents the characteristics of these components for each ODE-PDE.

Table 4: Training setup with optimization, loss and model settings

	Optimization				Loss				MH-PINN	
	l_r	γ	step-size	Epoch	ω_1	ω_2	N_1	N_2	Layer	Activation
OHO	0.0001	0.98	100	20000	1	1	512	1	[128, 128, 256]	<i>SiLU</i>
NCFE	0.0005	0.98	100	40000	1	1	512	1	[128, 128, 256]	<i>SiLU</i>
Duffing	0.0005	0.98	100	40000	1	1	512	1	[128, 128, 256]	<i>SiLU</i>
AR	0.0001	0.97	100	30000	10000	1	9376	483	[128, 128, 256, 256, 512]	<i>SiLU</i>

These parameters have been chosen empirically after hyper-parameter optimization. For ODEs, we used a NVIDIA GeForce GTX 1050 with 2GB of memory, and for PDEs, we used a Tesla V100-SXM2-16GB with 16GB of memory. A bigger model is used for AR because PDE requires more complexity, and a better GPU is used to reduce training computational time. To train AR, we used a 2D grid of (75, 125) so $N_1 = 75 \times 125 = 9376$ and used 201 collocation points for boundary conditions, 81 for initial conditions, so $N_2 = 2 * 201 + 81 = 483$.

F Scalability Analysis: Training Heads

In the following section, we provide the training head configurations of the STL-PINN scalability analysis. We trained multiple MH-PINNs with increasing ranges of α . The training head characteristics are reported in the tables below.

F.1 OHO

For every model and across all heads, the initial value is set as $y_0 = [1, 0.5]$.

Table 5: Scalability analysis for OHO: Stiff regimes of the training heads.

Model	Head	1	2	3	4	5	6	7	8	9	10
1	α	1	2	3	4	5	6	7	8	9	10
2	α	1	3	5	7	9	11	12	13	14	15
3	α	2	4	6	8	10	12	14	16	18	20
4	α	1	5	9	13	15	17	19	21	23	25

F.2 NCFE

For every model and across all heads, the initial value is set as $y_0 = [2, 4]$ and $\omega = 1$.

Table 6: Scalability analysis for NCFE: Stiff regimes of the training heads.

Model	Head	1	2	3	4	5	6	7	8	9	10
1	α	1	2	3	4	5	6	7	8	9	10
2	α	2	4	6	8	10	12	14	16	18	20
3	α	3	6	9	12	15	18	21	24	27	30

F.3 Duffing

For every model and across all heads, the initial value is set as $y_0 = [1, 0.5]$ and $\beta = 0.5$.

Table 7: Scalability analysis for Duffing: Stiff regimes of the training heads.

Model	Head	1	2	3	4	5	6	7	8	9	10
1	α	11	12	13	14	15	16	17	18	19	20
2	α	12	14	16	18	20	22	24	26	28	30
3	α	13	16	19	22	25	28	31	34	37	40

F.4 AR

For every model and across all heads, the initial value is set as $y_0^{max} = 1$.

Table 8: Scalability analysis for AR: Stiff regimes of the training heads.

Model	Head	1	2	3	4
1	α	1	2	3	4
2	α	3	6	9	12

G Reparametrization Analysis: Training Heads

We present the training head configurations of MH-PINN in a low-stiff regime of stiff-parameterized ODEs and PDE with varying initial conditions or forcing function. For OHO: y_{1_0} and $y_{2_0} \in [0, 5]$, Duffing: $y_{1_0} \in [0.5, 2]$ and $y_{2_0} \in [0, 1]$, AR equation: $y_0^{max} \in [0.5, 2]$, NCFE: $\omega \in [0, \pi]$ uniformly sample. Values are given with 2 C.S.

Table 9: Reparametrization Analysis: MH-PINN training heads

	Head	1	2	3	4	5	6	7	8	9	10
OHO	α	2	4	6	8	10	12	14	16	18	20
	y_{1_0}	0.59	1.1	1.4	2.9	3.7	4.2	4.1	0.30	2.2	1.7
	y_{2_0}	1.5	3.3	3.7	3.3	3.1	4.7	0.59	3.9	0.86	1.3
NCFE	α	2	4	6	8	10	12	14	16	18	20
	y_0	[2, 4]	[2, 4]	[2, 4]	[2, 4]	[2, 4]	[2, 4]	[2, 4]	[2, 4]	[2, 4]	[2, 4]
	ω	2.3	0.49	0.059	0.12	0.98	3.1	0.82	1.1	0.67	2.7
Duffing	α	13	16	19	22	25	28	31	34	37	40
	y_{1_0}	1.9	1.4	1.7	0.62	0.58	1.1	0.63	0.50	1.7	1.4
	y_{2_0}	0.59	0.62	0.19	0.32	0.34	0.81	0.51	0.26	0.81	0.43
	β	0.5	0.5	0.5	0.5	0.5	0.5	0.5	0.5	0.5	0.5
AR	α	3	6	8	12	-	-	-	-	-	-
	y_0^{max}	0.50	1.0	1.5	2.0	-	-	-	-	-	-

H Performance Analysis: Training and Transfer Learning Results

In this section, we give more figures about training and transfer learning. For each equation, we provide the results of a run, including the training loss curve, training head output, transfer learning solutions for $\alpha \in [10, 200]$ and the associated absolute error.

H.1 OHO

Here are the performance analysis, training and transfer results of the OHO equation.

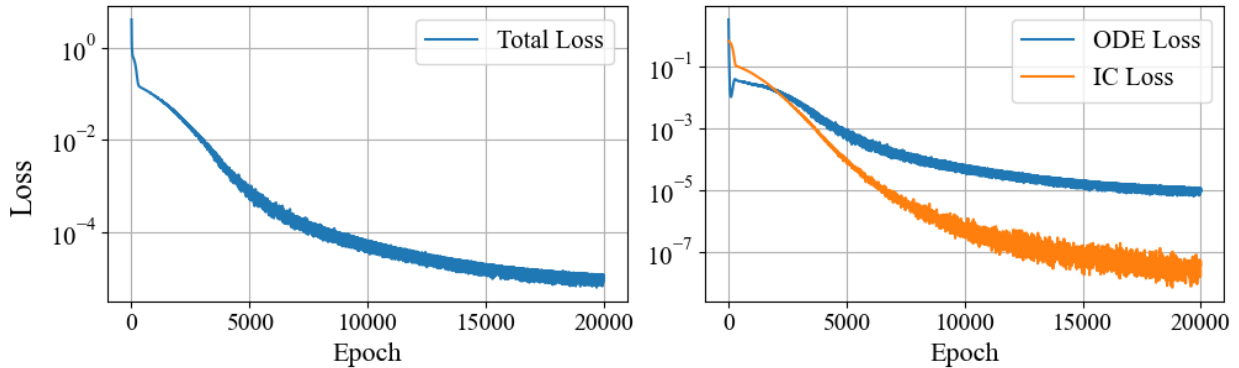


Figure 7: Training loss, along with the loss values for ODE and initial condition (IC), across epochs.

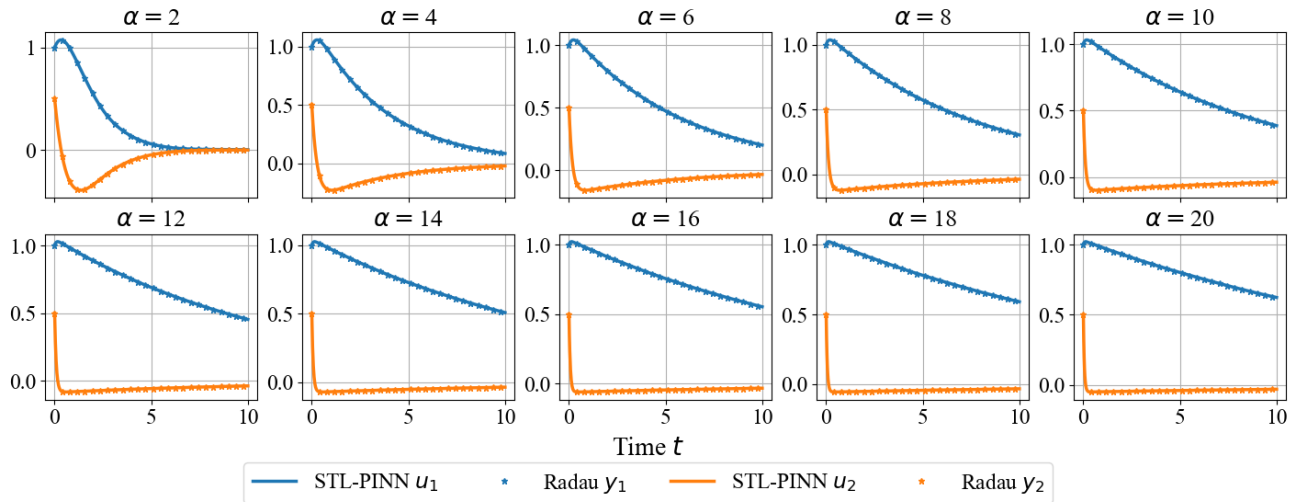


Figure 8: MH-PINN outcomes after training, along with the Radau numerical solution across all training heads.

From Figure 7 and Figure 8, we see that the network effectively learned the low-stiff solutions, as shown by the decreasing loss. Additionally, the numerical solutions closely align with MH-PINN solutions across all heads.

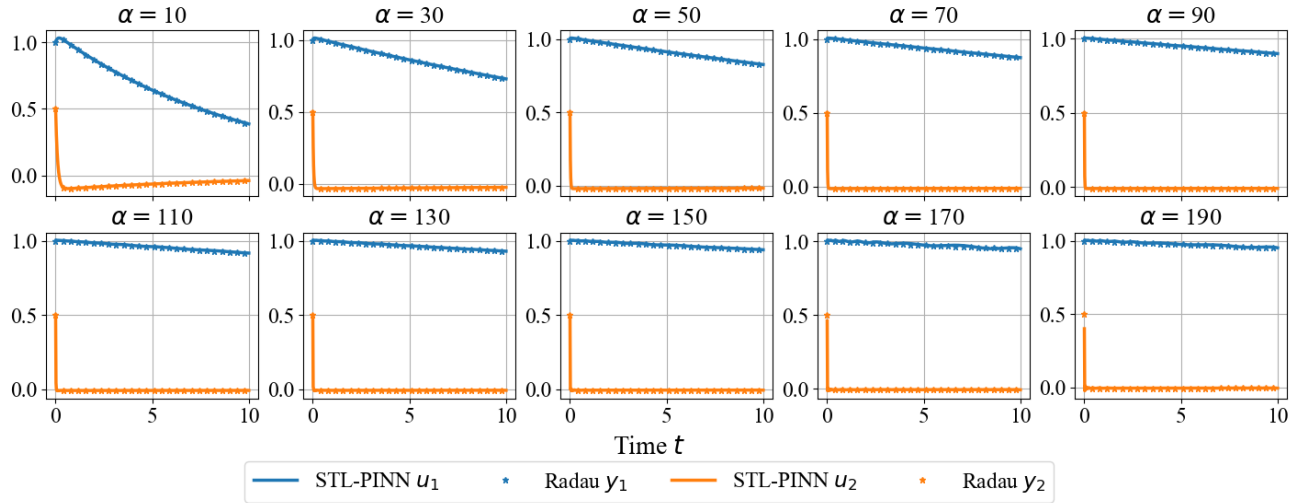


Figure 9: STL-PINN outcomes after transfer learning for $\alpha \in [10, 200]$, along with the Radau numerical solution.

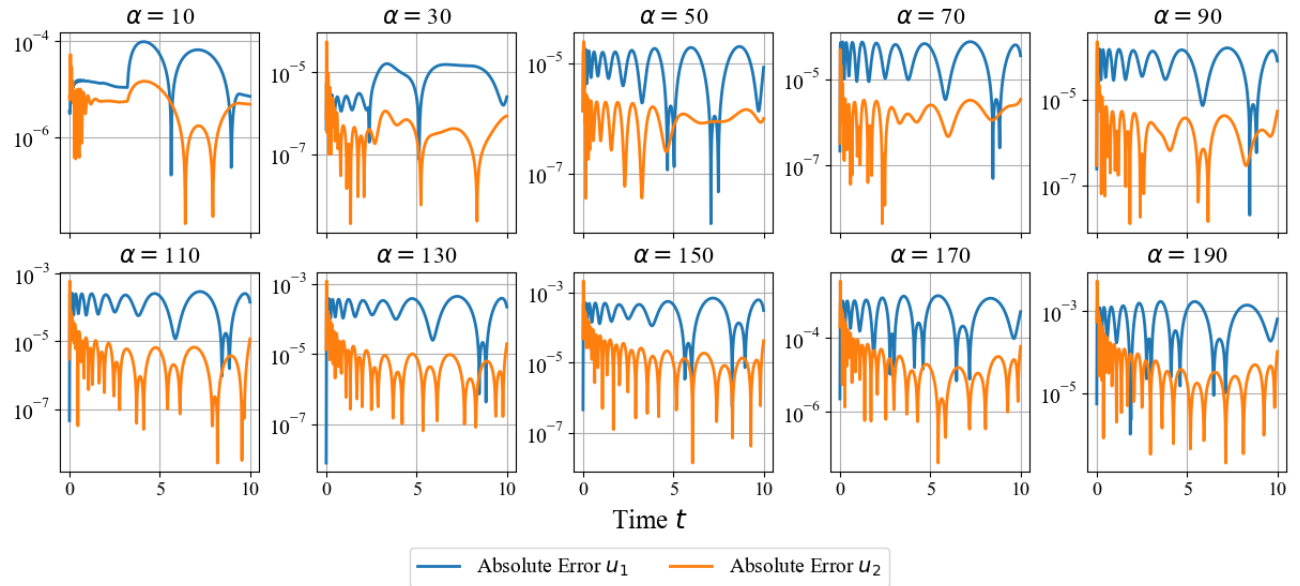


Figure 10: Absolute error of STL-PINN with respect to the Radau solution for $\alpha \in [10, 200]$.

Figure 9 and Figure 10 illustrate that STL-PINN can compute accurate solutions even in high-stiff regimes. It captures stiffness behaviors well, such as the transient phase near the initial condition of u_2 . However, errors increase with stiffness as we move further away from the low-stiff training regime.

H.2 NCFF

Here are the performance analysis, training and transfer results of the NCFF equation.

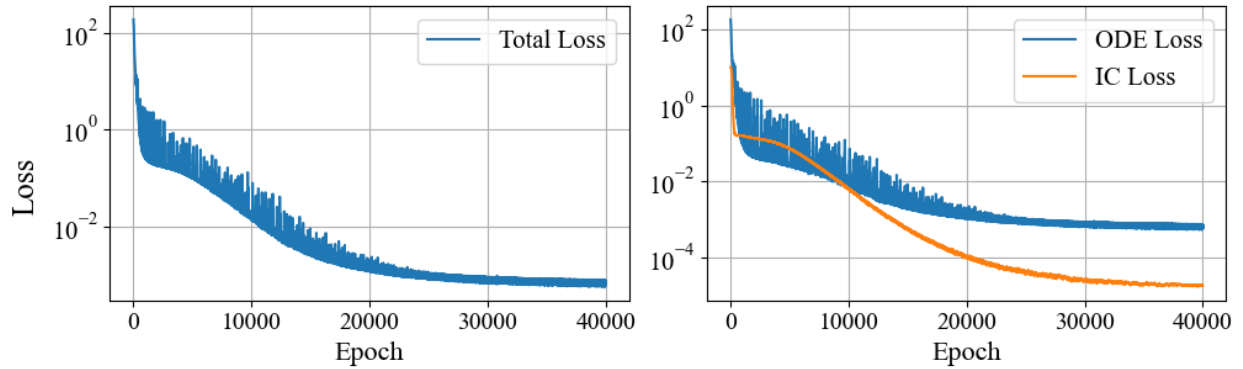


Figure 11: Training loss, along with the loss values for ODE and initial condition (IC), across epochs.

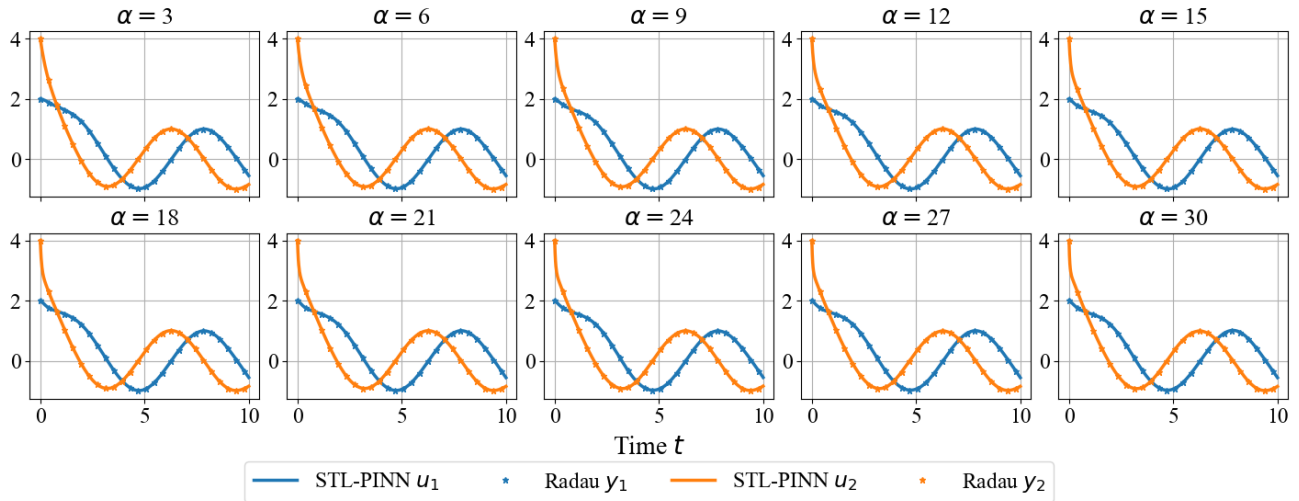


Figure 12: MH-PINN outcomes after training, along with the Radau numerical solution across all training heads.

From Figure 11 and Figure 12, we see that the network effectively learned the low-stiff solutions, as shown by the decreasing loss. Additionally, the numerical solutions closely align with MH-PINN solutions across all heads.

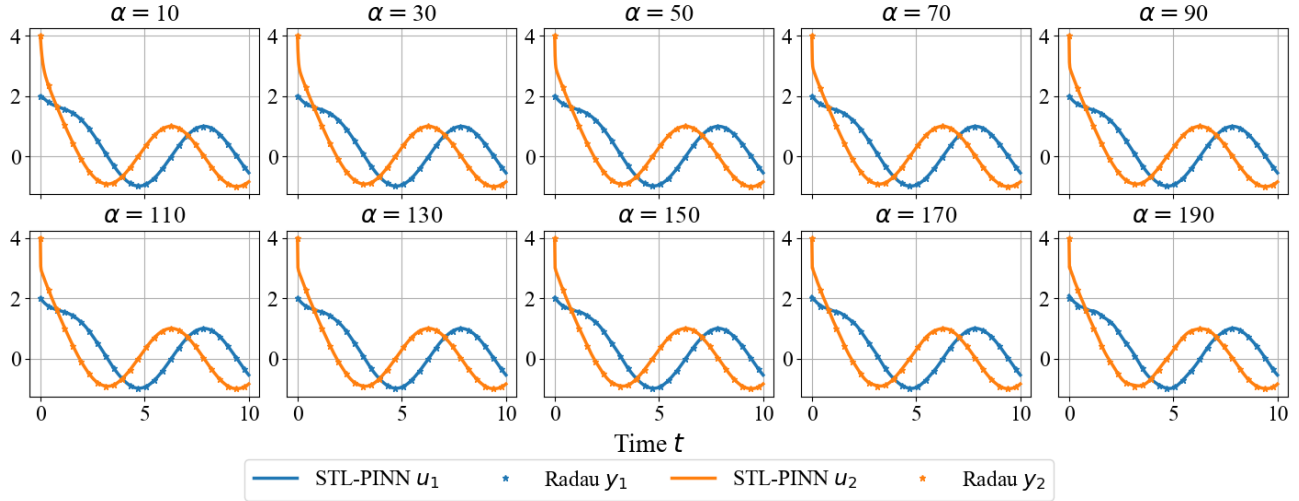


Figure 13: STL-PINN outcomes after transfer learning for $\alpha \in [10, 200]$, along with the Radau numerical solution.

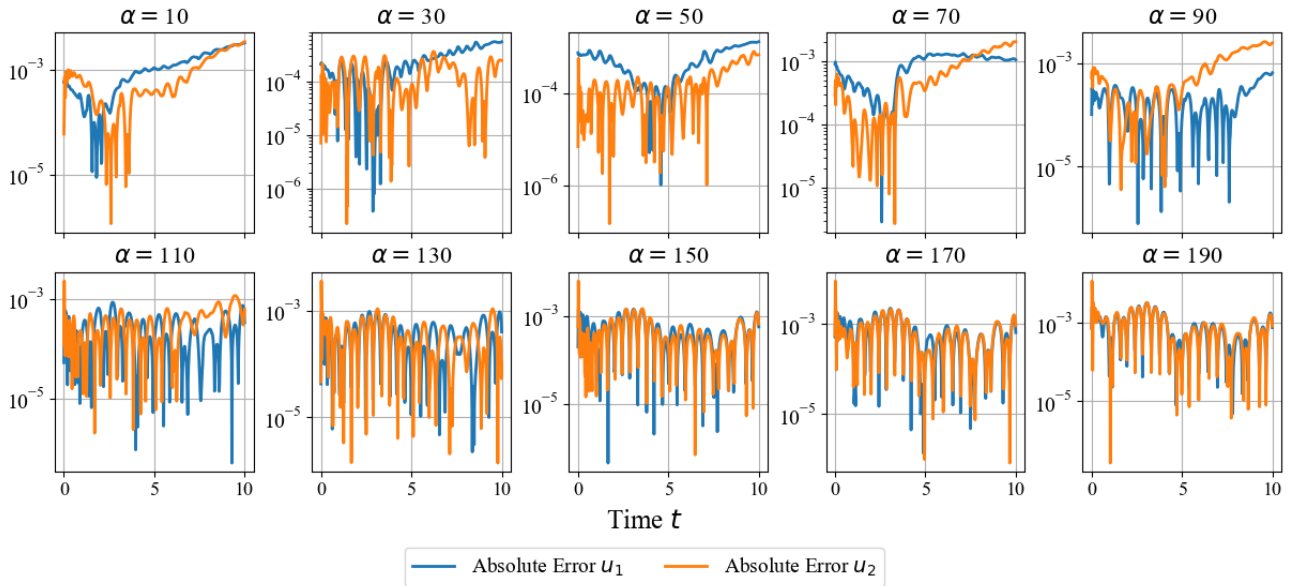


Figure 14: Absolute error of STL-PINN with respect to the Radau solution for $\alpha \in [10, 200]$.

Figure 13 and Figure 14 illustrate that STL-PINN can compute accurate solutions even in high-stiff regimes. It captures stiffness behaviors well, such as the transient phase near the initial condition of u_2 . However, errors increase with stiffness as we move further away from the low-stiff training regime.

H.3 Duffing

Here are the performance analysis, training and transfer results of the Duffing equation.

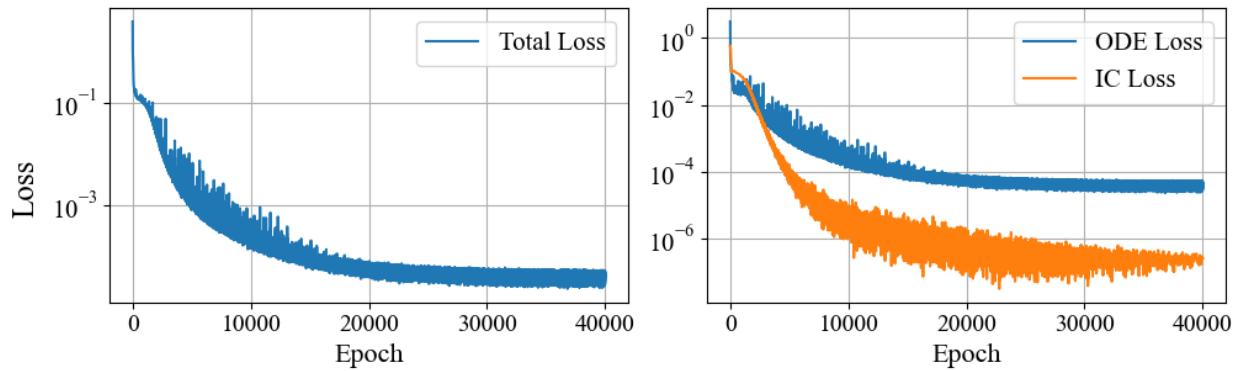


Figure 15: Training loss, along with the loss values for ODE and initial condition (IC), across epochs.

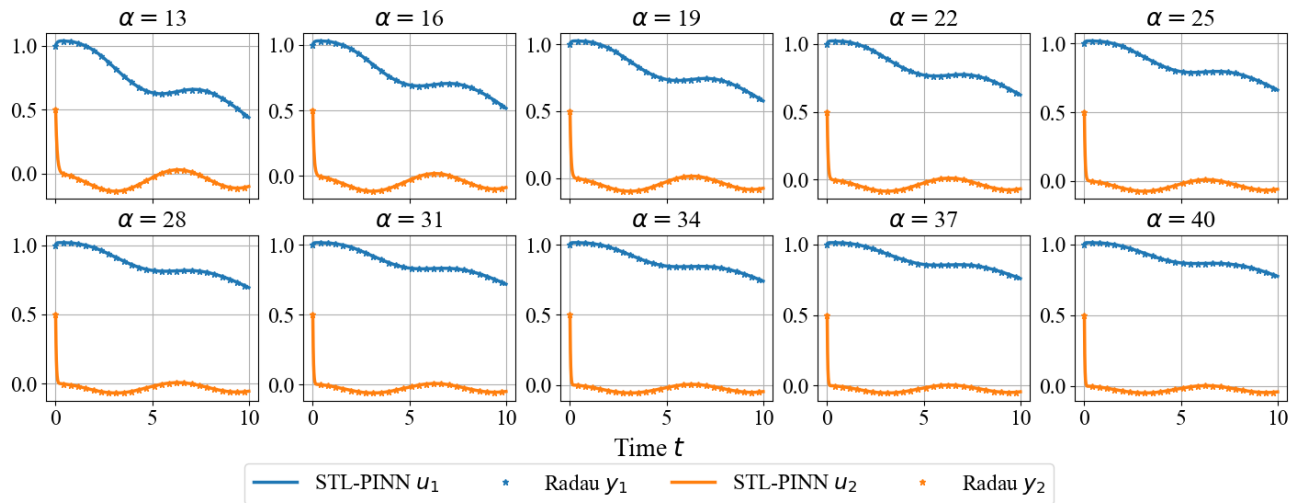


Figure 16: MH-PINN outcomes after training, along with the Radau numerical solution across all training heads..

For the Duffing equation, MH-PINNs is trained on its linear form, as the nonlinear part is then approximated during transfer learning with the perturbation expansion. Here, the training results are given for the linear form of the equation. From Figure 15 and Figure 16, it's clear that the network effectively learned the low-stiff solutions, as shown by the decreasing loss. Additionally, the numerical solutions closely align with MH-PINN solutions across all heads.

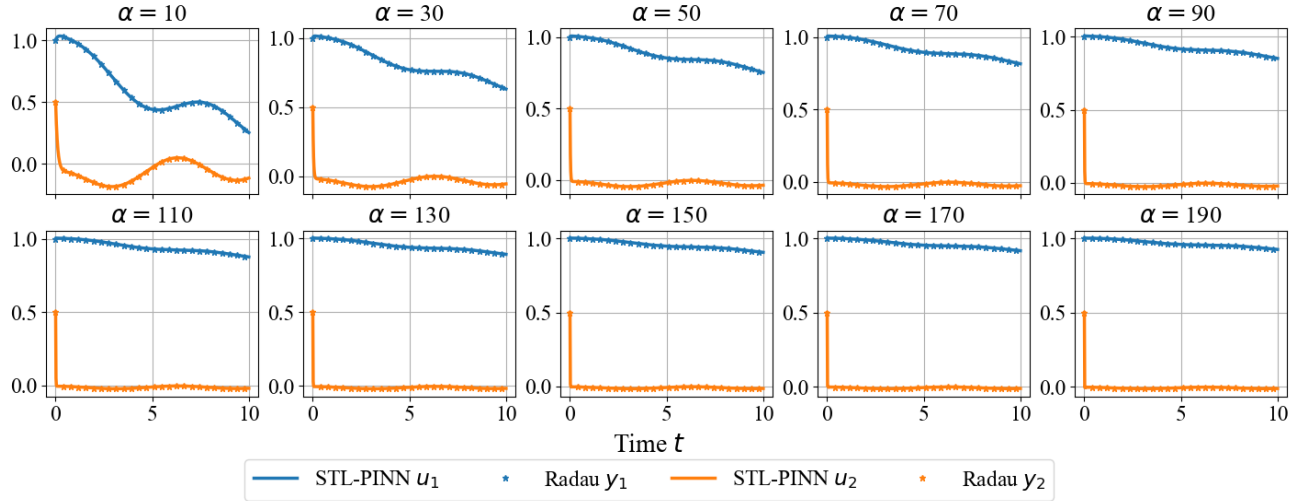


Figure 17: STL-PINN outcomes after transfer learning for $\alpha \in [10, 200]$, along with the Radau numerical solution.

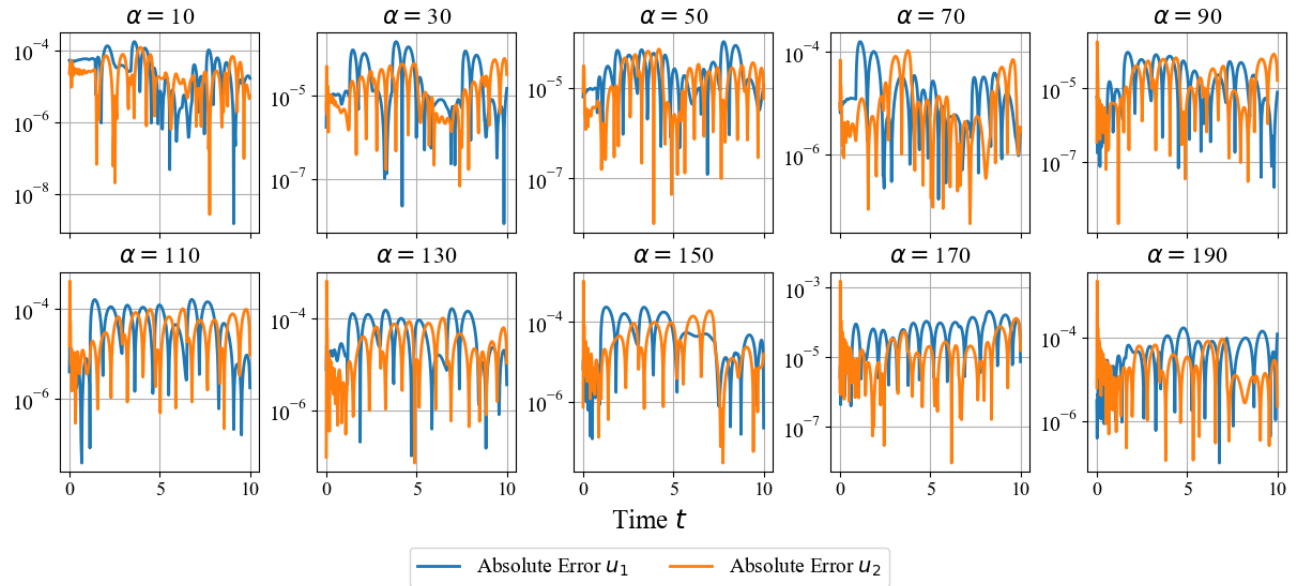


Figure 18: Absolute error of STL-PINN with respect to the Radau solution for $\alpha \in [10, 200]$.

Here, we present the transfer learning results on the nonlinear form using the perturbation expansion. Figure 17 and Figure 18 illustrate that STL-PINN can compute accurate solutions even in high-stiff regimes. It also effectively approximates the nonlinearity through the perturbation expansion. It captures stiffness behaviors well, such as the transient phase near the initial condition of u_2 . However, errors increase with stiffness as we move further away from the low-stiff training regime.

H.4 AR

Here are the performance analysis, training and transfer results of the AR equation.

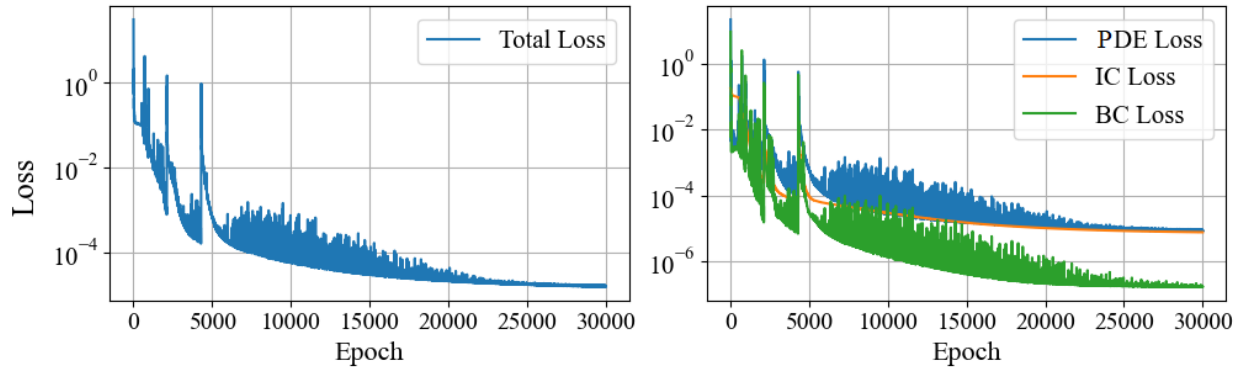


Figure 19: Training loss, along with the loss values for ODE and initial condition (IC) and boundary condition (BC) across epochs.

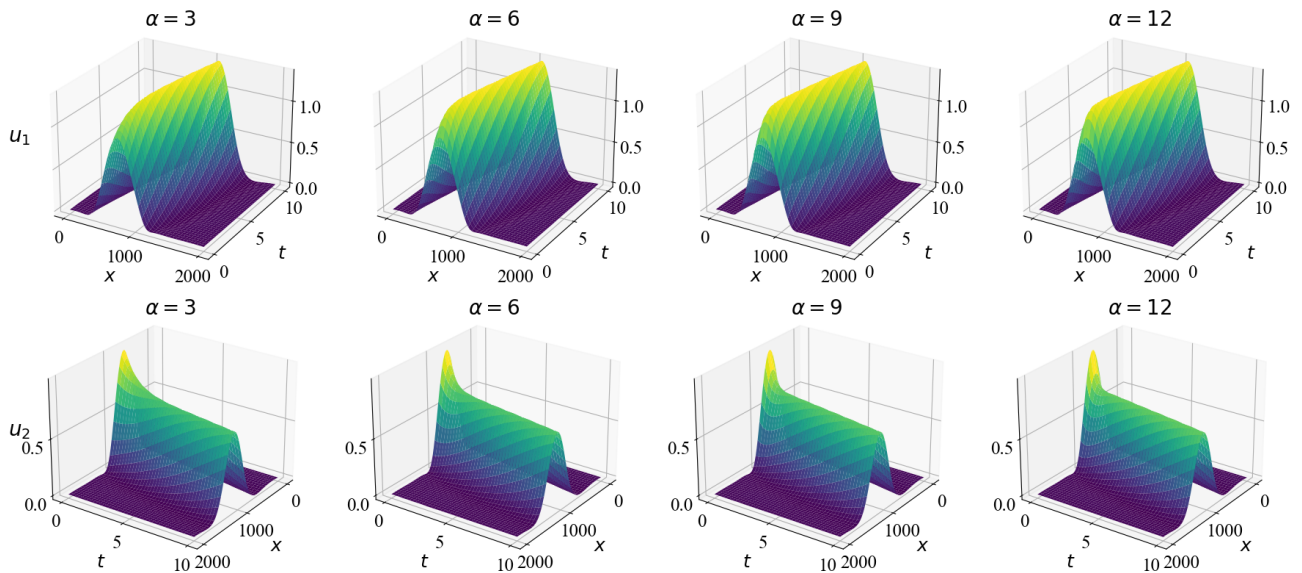


Figure 20: MH-PINN outcomes after training across all training heads.

From Figure 19 and Figure 20, we see that the network effectively learned the low-stiff solutions, as shown by the decreasing loss even for the boundary and initial conditions. We observe that u_1 and u_2 correctly reach equilibrium after a relatively slow transient phase due to the low stiffness regimes.

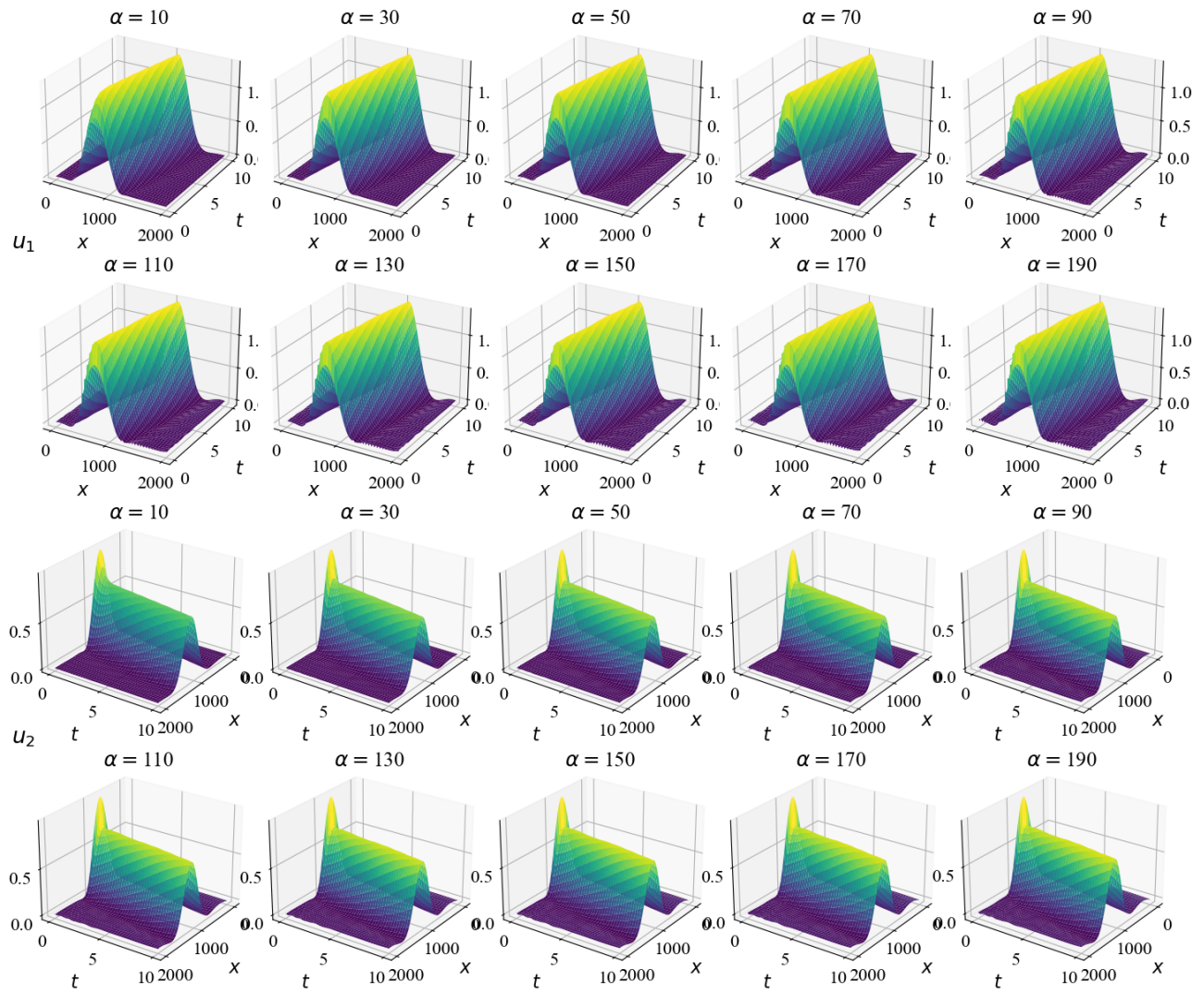


Figure 21: STL-PINN outcomes after transfer learning for $\alpha \in [10, 200]$.

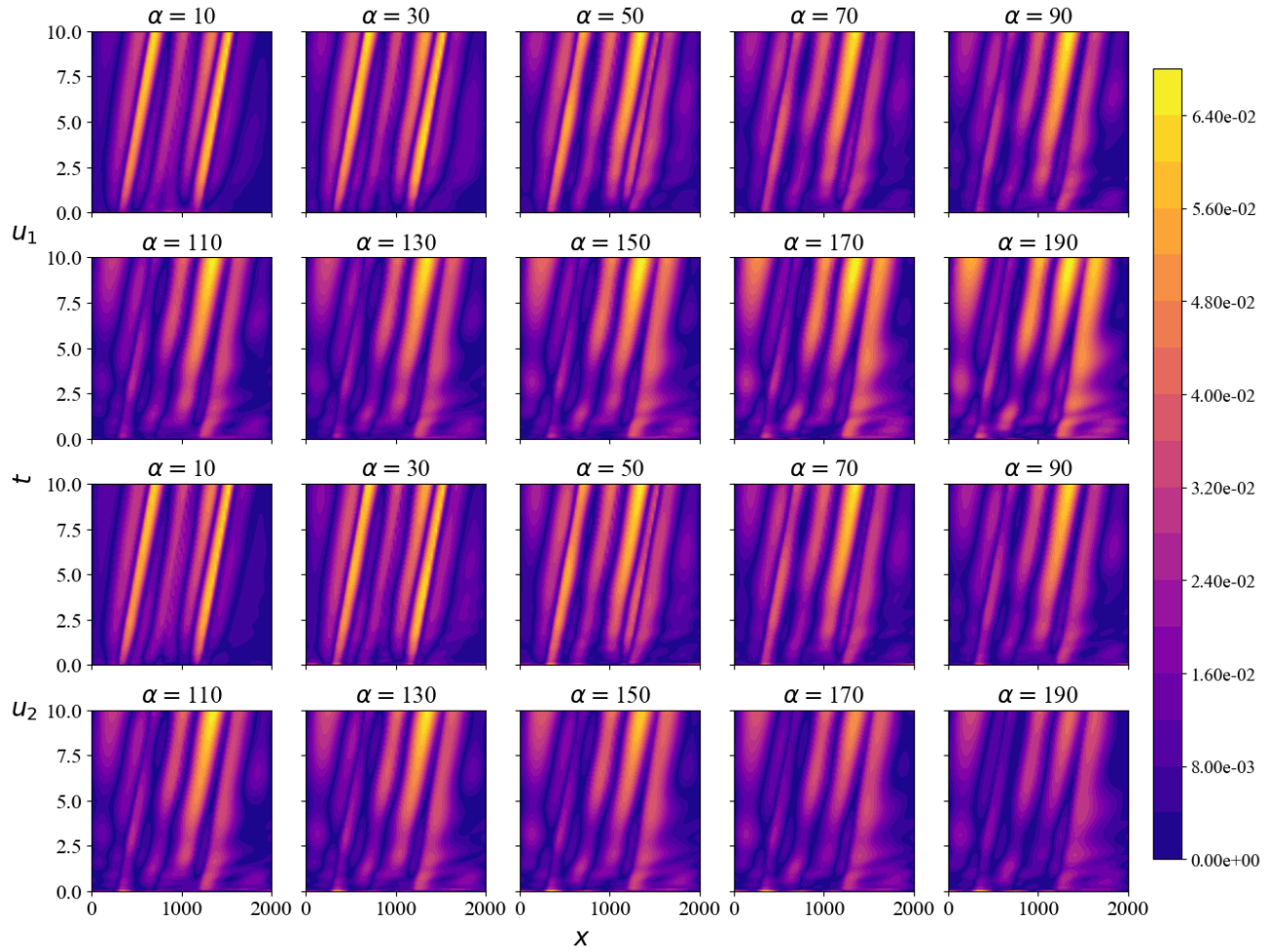


Figure 22: Absolute error of STL-PINN with respect to the LW-Radau solution for $\alpha \in [10, 200]$.

Figure 21 and Figure 22 illustrate that STL-PINN can compute accurate PDEs solutions even in high-stiff regimes. Transient phases are now very rapid, with solutions reaching equilibrium quickly. However, errors increase with stiffness as we move further away from the low-stiff training regime.

I Performance Analysis: More Metrics

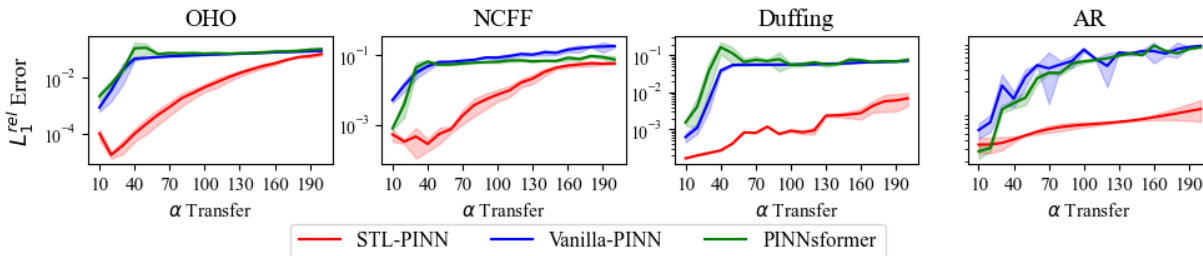


Figure 23: L_1 relative error over vanilla PINN, PINNsFormer and STL-PINN solving stiff-parameterized ODEs-PDEs as stiffness regime increases, with $\alpha \in [10, 200]$. The reported errors are the average of three separate runs, along with 90% confidence intervals.

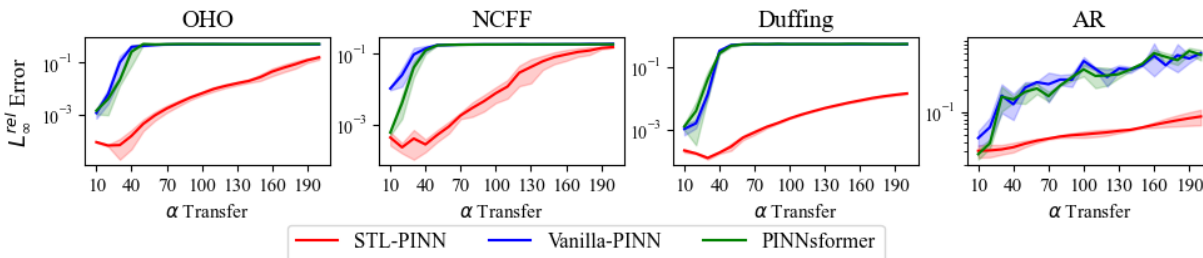


Figure 24: L_∞ relative error of vanilla PINN, PINNsFormer and STL-PINN solving stiff-parameterized ODEs-PDEs as stiffness regime increases, with $\alpha \in [10, 200]$. The reported errors are the average of three separate runs, along with 90% confidence intervals.

Here, Figure 23 and 24 show L_1 relative error and L_∞ relative error of the performance analysis. STL-PINN consistently outperforms vanilla PINNs and PINNsFormer methods across all α values.

J Scalability Analysis: More Metrics

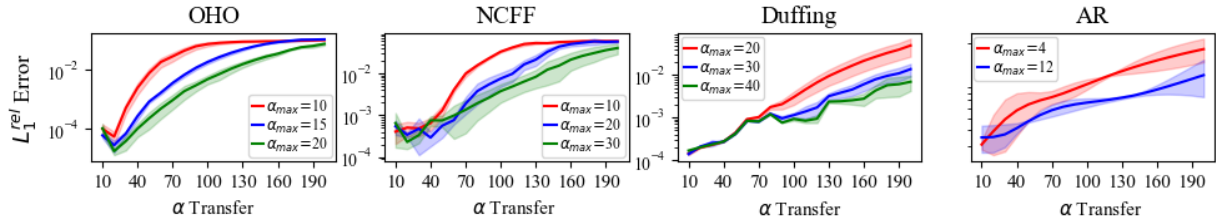


Figure 25: L_1 relative error of STL-PINN over increasing ranges of α during training, where α_{max} denotes the maximum value. The x-axis is the α transfer range. The reported errors are the average of three separate runs, along with 90% confidence intervals.

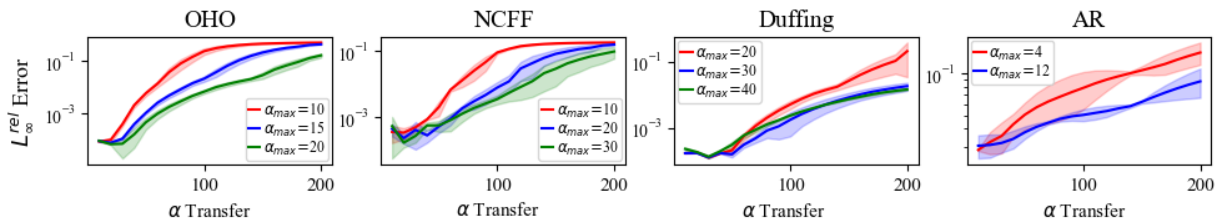


Figure 26: L_∞ relative error of STL-PINN over increasing ranges of α during training, where α_{max} denotes the maximum value. The x-axis is the α transfer range. The reported errors are the average of three separate runs, along with 90% confidence intervals.

Here, Figure 25 and 26 show L_1 relative error and L_∞ relative error of the scalability analysis. As mentioned in the result section, it demonstrates the scalability of our method: the more we train in stiff regimes, the more we extend the range of transfer learning to even stiffer regimes.

K Reparametrization Analysis: Training Results

In this section, we give figures about training results of the reparametrization analysis. For each equation, we provide the training outcomes including training loss curve and training head output.

K.1 OHO

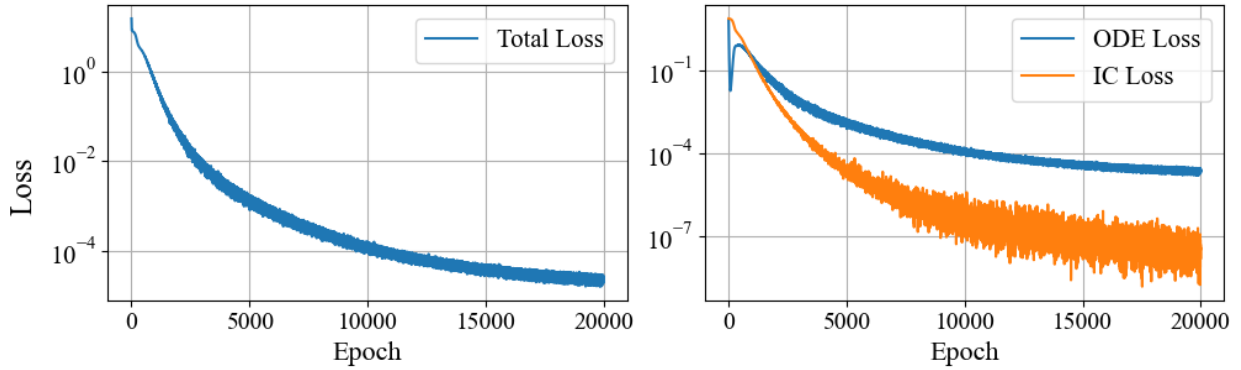


Figure 27: Training loss of the reparametrization analysis, along with the loss values for ODE and initial condition (IC), across epochs.

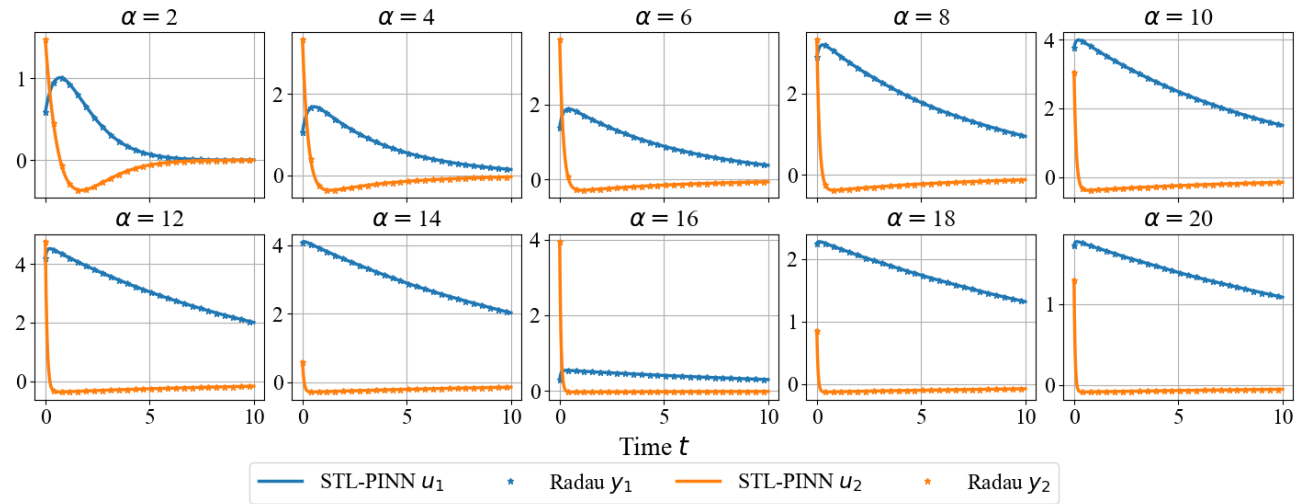


Figure 28: MH-PINN outcomes after training with different initial conditions, along with the Radau numerical solution over the 10 heads.

Figures 27 and 28 show that the network effectively learned solutions with various initial conditions, as shown by the decreasing loss. Additionally, the numerical solutions closely align with MH-PINN solutions across all heads, successfully encoding the different initial conditions.

K.2 NCFF

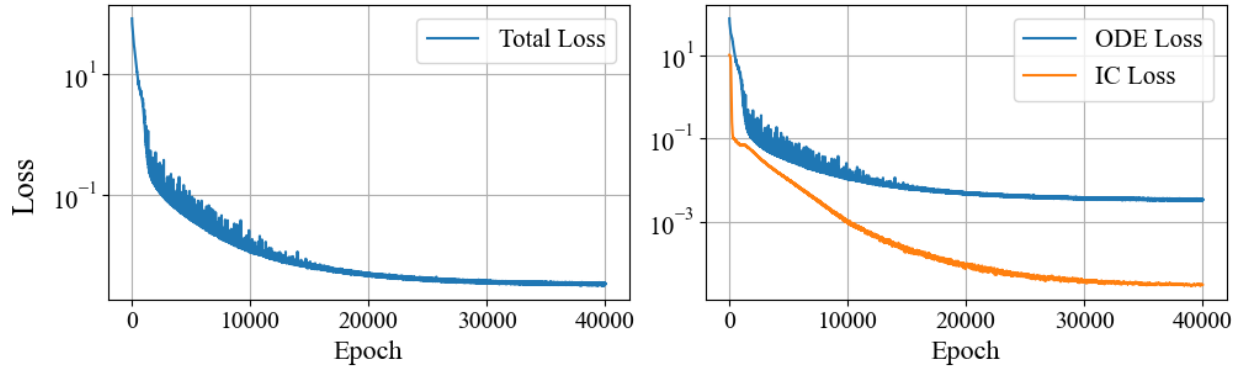


Figure 29: Training loss of the reparametrization analysis, along with the loss values for ODE and initial condition (IC), across epochs.

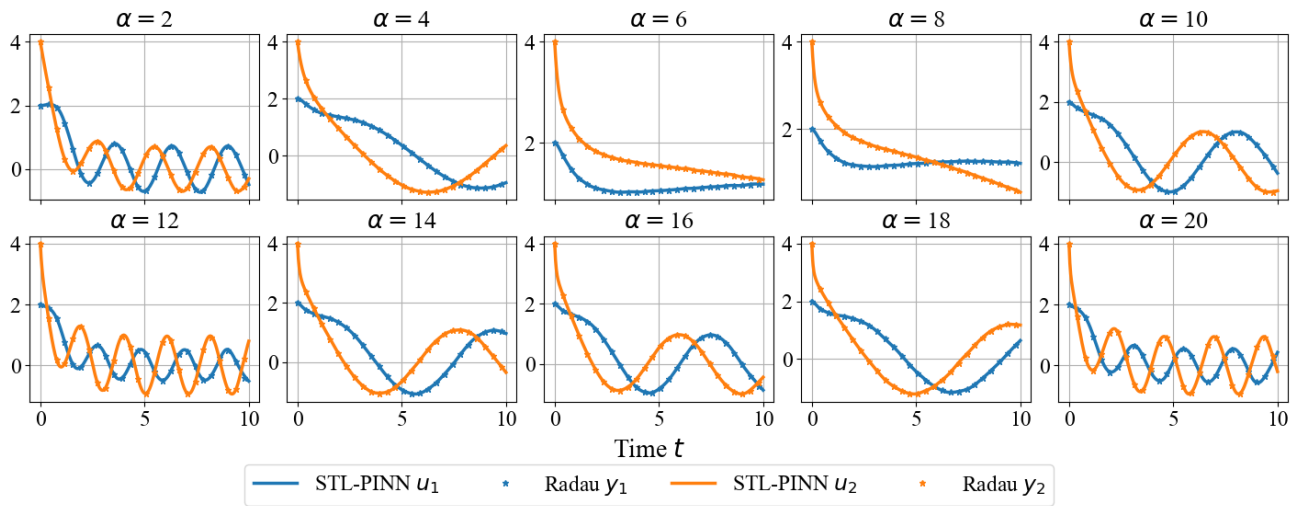


Figure 30: MH-PINN outcomes after training with different forcing functions, along with the Radau numerical solution over the 10 heads.

Figures 29 and 30 show that the network effectively learned solutions with various forcing functions, as shown by the decreasing loss. Additionally, the numerical solutions closely align with MH-PINN solutions across all heads, successfully encoding the different forcing functions.

K.3 Duffing

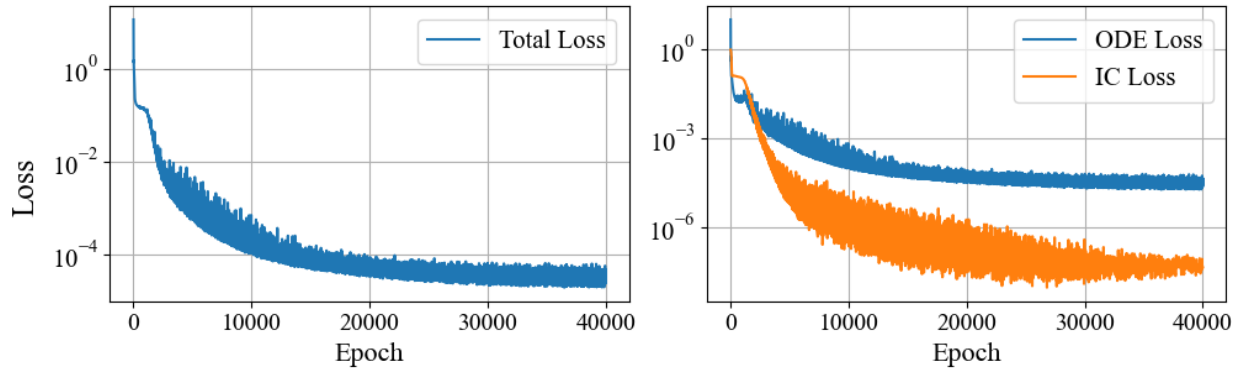


Figure 31: Training loss of the reparametrization analysis, along with the loss values for ODE and initial condition (IC), across epochs.

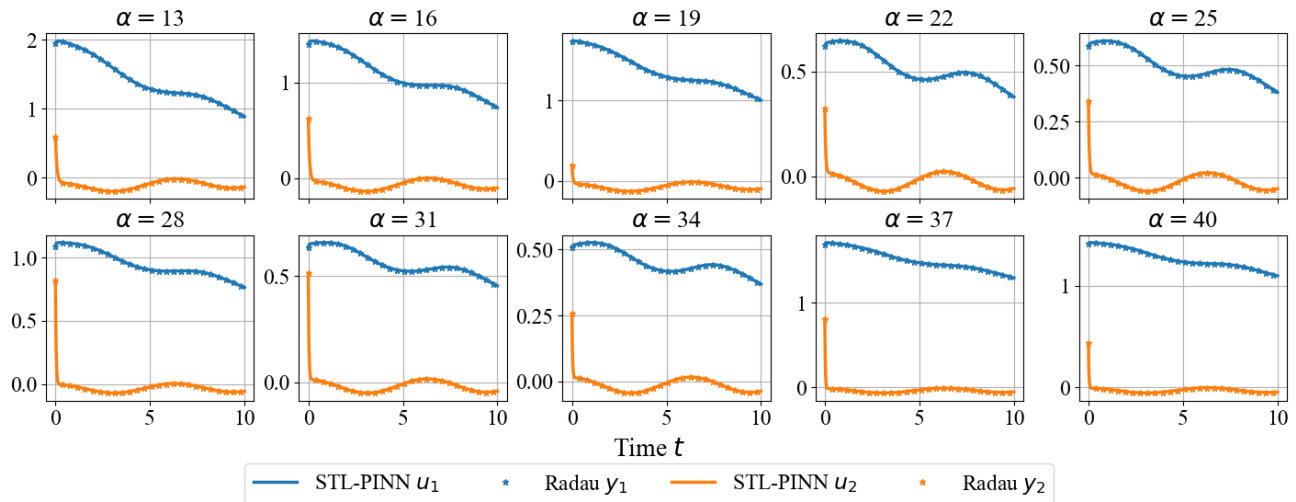


Figure 32: MH-PINN outcomes after training with different initial condition, along with the Radau numerical solution over the 4 heads.

For the Duffing equation, MH-PINNs are trained on its linear form, as the nonlinear part is then approximated during transfer learning with the perturbation expansion. Here, the training results are given for the linear form of the equation. Figures 31 and 32 show that the network effectively learned solutions with various initial conditions, as shown by the decreasing loss. Additionally, the numerical solutions closely align with MH-PINN solutions across all heads, successfully encoding the different initial conditions.

K.4 AR

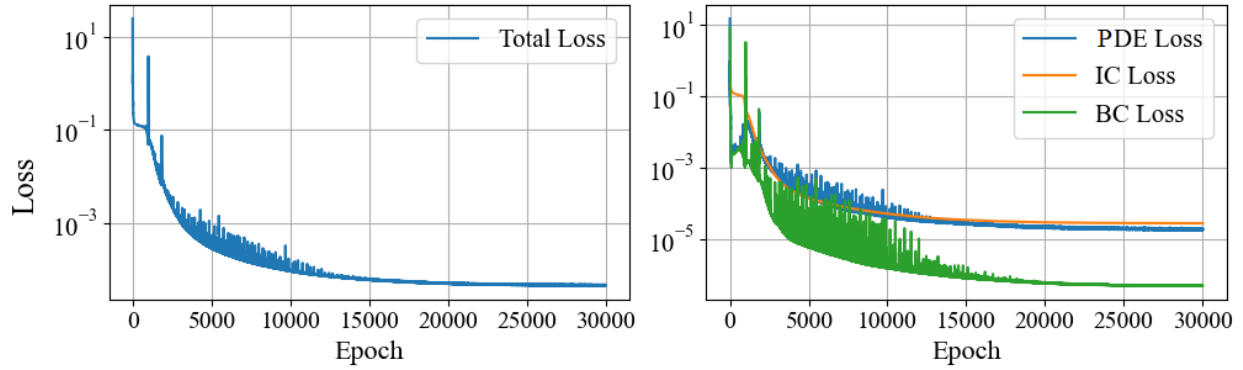


Figure 33: Training loss of the reparametrization analysis, along with the loss values for ODE, initial condition (IC) and boundary condition (BC), across epochs.

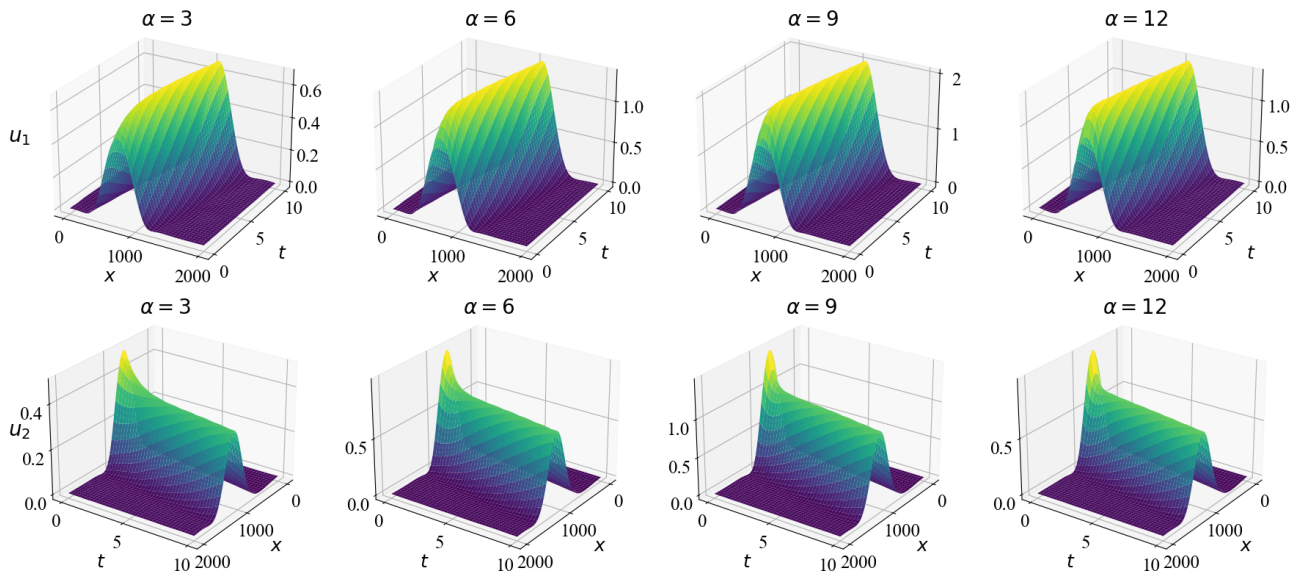


Figure 34: MH-PINN outcomes after training with different initial condition, over the 4 heads.

From Figure 33 and Figure 34, we see that the network effectively learned the low-stiff solutions with various initial conditions, as shown by the decreasing loss.